Atmos. Chem. Phys. Discuss., 15, 22715–22779, 2015
www.atmos-chem-phys-discuss.net/15/22715/2015/
doi:10.5194/acpd-15-22715-2015

Atmospheric Chemistry and Physics Discussions

Investigation of error sources in regional inverse estimates of greenhouse gas emissions in Canada

E. Chan[1], D. Chan[1], M. Ishizawa[2], F. Vogel[3], J. Brioude[4,5], A. Delcloo[6], Y. Wu[7], and B. Jin[8]

[1]Environment Canada, Climate Research Division, Toronto, Ontario, Canada
[2]National Institute for Environmental Studies, Center for Global Environmental Research, Tsukuba, Japan
[3]Laboratoire des Sciences du Climat et de l'Environnement, Chaire BridGES, Gif-sur-Yvette, France
[4]NOAA Earth System Research Laboratory, Chemical Sciences Division, Boulder, Colorado, USA
[5]University of Colorado, Cooperative Institute for Research in Environmental Sciences, Boulder, Colorado, USA
[6]Royal Meteorological Institute of Belgium, Uccle, Belgium
[7]York University, Mathematics and Statistics, Toronto, Ontario, Canada
[8]University of Science and Technology of China, Statistics and Finance, Hefei, Anhui, China

Received: 24 June 2015 – Accepted: 21 July 2015 – Published: 26 August 2015

Correspondence to: E. Chan (elton.chan@ec.gc.ca)

Published by Copernicus Publications on behalf of the European Geosciences Union.

ACPD
15, 22715–22779, 2015

Abstract

Inversion models can use atmospheric concentration measurements to estimate surface fluxes. This study is an evaluation of the errors in a regional flux inversion model for different provinces of Canada, Alberta (AB), Saskatchewan (SK) and Ontario (ON). Using CarbonTracker model results as the target, the synthetic data experiment analyses examined the impacts of the errors from the Bayesian optimisation method, prior flux distribution and the atmospheric transport model, as well as their interactions. The scaling factors for different sub-regions were estimated by the Markov chain Monte Carlo (MCMC) simulation and cost function minimization (CFM) methods. The CFM method results are sensitive to the relative size of the assumed model-observation mismatch and prior flux error variances. Experiment results show that the estimation error increases with the number of sub-regions using the CFM method. For the region definitions that lead to realistic flux estimates, the numbers of sub-regions for the western region of AB/SK combined and the eastern region of ON are 11 and 4 respectively. The corresponding annual flux estimation errors for the western and eastern regions using the MCMC (CFM) method are −7 and −3 % (0 and 8 %) respectively, when there is only prior flux error. The estimation errors increase to 36 and 94 % (40 and 232 %) resulting from transport model error alone. When prior and transport model errors coexist in the inversions, the estimation errors become 5 and 85 % (29 and 201 %). This result indicates that estimation errors are dominated by the transport model error and can in fact cancel each other and propagate to the flux estimates non-linearly.

In addition, it is possible for the posterior flux estimates having larger differences than the prior compared to the target fluxes, and the posterior uncertainty estimates could be unrealistically small that do not cover the target. The systematic evaluation of the different components of the inversion model can help in the understanding of the posterior estimates and percentage errors. Stable and realistic sub-regional and monthly flux estimates for western region of AB/SK can be obtained, but not for the eastern region of ON. This indicates that it is likely a real observation-based inversion for the

ACPD
15, 22715–22779, 2015

annual provincial emissions will work for the western region whereas; improvements are needed with the current inversion setup before real inversion is performed for the eastern region.

1 Introduction

Environment Canada's Greenhouse Gas Measurement Program currently operates a network of ground-based stations to accurately measure atmospheric mole fractions of greenhouse gases in Canada. Inversion studies have used GHG network observations to estimate sources and sinks of GHG emissions in context of nationally reported emissions. There have been a large number of inverse modelling studies focusing on Europe (e.g. Bergamaschi et al., 2005, 2010; Rigby et al., 2011) and the US (e.g. Zhao et al., 2009; Jeong et al., 2012; Brioude et al., 2011, 2012, 2013; Miller et al., 2013). Global inversion systems such as CarbonTracker which estimate the sources and sinks of CO_2 and CH_4 (Bruhwiler et al., 2014) could also be applied to Canada. These global inversions however, are only able to resolve fluxes at the sub-continental scales. On the regional scale, i.e., on the scale of a province or territory, large discrepancies were found in the flux estimates and spatial distributions among studies (e.g. Vogel et al., 2012; Miller et al., 2013). The sources of uncertainties in inversion models can be studied more systematically with synthetic data experiments with known fluxes. This is the motivation for this study in which we assess our inverse modelling approach to estimate regional annual fluxes. The scientific goal is to estimate GHG fluxes that can be used to verify the bottom-up inventory estimates focusing on Canada taking advantage of the wealth of EC's measurement data already available.

The continental continuous surface atmospheric concentrations (mole fractions) of GHG observations exhibit strong synoptic (over a few days) variations that (partly) reflect the transport of emissions from the surrounding regions. Lagrangian particle dispersion models with footprints typically on the order of 10^6 km^2 in size (Gloor et al.,

ACPD
15, 22715–22779, 2015

2001) are potentially applicable for the identification of source regions and quantification of emissions responsible for the observed synoptic variations.

Typically the regional atmospheric inversion studies employ Lagrangian particle dispersion models driven by modelled meteorology to simulate the transport of the chemical species, combined with prior emission distributions to yield modelled mole fractions at the measurement station(s), and then the emissions are "optimized" to minimize the modelled-observed mole fraction differences. These inversion studies vary widely in their spatial and temporal domains (10^4 to 10^6 km^2 spatially, days to annual temporally), other differences include inference of spatial distribution of emissions and/or relative strength of different source types, etc.

With the goal of developing an inversion modelling approach to apply over Canada, we characterise the sensitivity and limitations of the various components/aspects of the inversion model using a series of synthetic observation experiments that allow us to investigate the impacts associated with individual and combined errors. We report here on the inversion estimation errors and uncertainties associated with prior fossil fuel CO_2 flux errors, atmospheric transport model errors, optimisation schemes, the sensitivity to the number of source regions optimized, as well as combinations of these uncertainties.

A Bayesian inversion approach for atmospheric applications that incorporates prior fluxes and their associated first guess uncertainties was applied to CO_2 in Enting et al. (1993, 1995) and Fan et al. (1998, 1999). Since then a large number of atmospheric GHG inversion studies spanning over the last two decades (Gerbig et al., 2003; Kort et al., 2008; Stohl et al., 2009; Zhao et al., 2009; Bergamaschi et al., 2010; Manning et al., 2011; Thompson et al., 2011; Tolk et al., 2011; Jeong et al., 2012; Cressot et al., 2014) have applied one of the cost function minimization techniques to minimize the difference between observations and modelled mole fractions to obtain a set of optimal estimates either for scaling the prior fluxes in space or scaling some process parameters. In Brioude et al. (2011), an improvement of the cost function method was introduced by using an iterative method to find the median of the posterior distribution

ACPD
15, 22715–22779, 2015

instead of the mean. When positive (net) fluxes were expected, their method was not required to impose any non-negativity constraints on the covariance matrices to ensure positive flux results.

Two widely used approaches are the ensemble and the variational methods. This study uses both the Markov chain Monte Carlo (MCMC) method as an ensemble method and the cost function minimization method (CFM) which is considered a batch variational method in which a cost function is involved. Rigby et al. (2011) was one of the few who implemented the MCMC method in flux inversion studies. Miller et al. (2014) compared several approaches under a synthetic study and concluded that the MCMC methods produced the most realistic estimates and confidence intervals with known bounds. They pointed out inverse modelling approaches based on Gaussian assumptions could not incorporate such bounds and often produced unrealistic results. For example, emission grids or regions may have known physical constraints (e.g. non-negative emissions).

The term "posterior error" will be used wherever appropriate throughout the text to represent the estimation error compared to a known target, the contributions and the interaction of the different error components including the errors of the inversion procedure, prior flux and transport model are examined using sensitivity experiments. However, in the real observations-based inversion, the magnitude and sign of the errors and bias are often not known and treated as part of the total estimation uncertainty. This study will show that uncertainty estimates could often be unrealistically small and this issue of estimation bias and posterior uncertainties needs to be closely examined in any inversion study.

2 Methods

In this study, the components of atmospheric inversion using simulations run in a backward (adjoint) mode are the (synthetic) observations, a Lagrangian particle dispersion model (LPDM), meteorological modelled fields from a meteorological model as the

ACPD
15, 22715–22779, 2015

input to drive the LPDM, prior (a priori) spatial distributions of emissions, a method to estimate the baseline (background influence) of the observations, and a statistical technique to minimize any differences between modelled and observations of mole fractions. In this study, the observed atmospheric CO_2 mole fractions were not used, instead, (synthetic) observations were simulated from monthly fossil fuel CO_2 fluxes that were extracted from the outputs of the global model NOAA CarbonTracker release version 2011 (CT2011). Figure 1 shows a schematic of one set (IV) of inversion experiments. The impacts of the components to the flux estimates as highlighted in gray boxes are the focus of this study. The details are described in the following subsections.

2.1 Observation stations and inversion domains

Seven surface GHG monitoring stations were selected as a test bed for evaluating the inverse modelling approach. These seven stations (Table 1) in Alberta, Saskatchewan and Ontario represent regions which include the major Canadian anthropogenic GHG emissions. In 2012, CO_2 contributed 79 % of Canada's total GHG emissions that were estimated to be 699 megatonnes (Mt) of CO_2 equivalent (Environment Canada, 2012). The majority of these emissions resulted from the combustion of fossil fuels and the remaining portions were contributed from industrial processes and waste incinerations. These seven GHG stations are located in the three Canadian provinces that contributed close to 70 % of the national total GHG emissions annually according to the GHG national inventory of Canada (Environment Canada, 2012).

In this study, the inversion was done separately for the western region of Alberta and Saskatchewan provinces and the eastern region of Ontario. As shown in Fig. 2a–g, seven region definitions were used in this study to define sub-regions to be optimized; (2a) two sub-regions for the provinces of Alberta/Saskatchewan (AB/SK), one sub-region for the province of Ontario (ON), (2b) four sub-regions for AB/SK, two sub-regions for ON, (2c) seven sub-regions for AB/SK, four sub-regions for ON, (2d) eleven sub-regions for AB/SK, six sub-regions for ON, (2e) nineteen sub-regions for AB/SK,

ACPD
15, 22715–22779, 2015

twelve sub-regions for ON, (2f) twenty-seven sub-regions for AB/SK, twenty-four sub-regions for ON, and (2g) thirty-seven sub-regions (census divisions) for AB/SK and forty-nine sub-regions (census divisions) for ON to investigate whether there are problems and/or benefits (magnitude of biases and uncertainties) of estimating a large number of parameters.

2.2 Prior fluxes

Two sets of fossil fuel CO_2 fluxes were used as prior and target (known "truth") fluxes and summarized in Table 2, which includes the monthly and annual provincial totals from CT2010 and CT2011 fossil fuel CO_2. The fluxes were uniformly re-distributed to $0.2^\circ \times 0.2^\circ$ from the original resolution of $1^\circ \times 1^\circ$ to be folded into the emission sensitivity fields from FLEXPART (next section). For visualization, the gridded fluxes were aggregated into sub-regions to be optimized as shown in Fig. 2. Year 2009 country and global totals (by fuel type) were extrapolated from the 2007 Carbon Dioxide Information Analysis Center (CDIAC, Boden et al., 2013) used for the CT2010 fossil fuel fluxes (CarbonTracker, 2010). Open-source Data Inventory for Anthropogenic CO_2 (ODIAC, Oda and Maksyutov, 2011) emissions are spatially distributed using many available "proxy data" that explain spatial extent of emissions according to emission types (emissions over land, gas flaring, aviation and marine bunker). CarbonTracker combined the ODIAC emissions with CDIAC emissions to generate CT2011 fossil fuel fluxes (Andres et al., 2011; CarbonTracker, 2011). Note that CT2011 is half CDIAC plus half ODIAC, and ODIAC has different spatial distribution than CDIAC.

2.3 Transport

The European Centre for Medium-range Weather Forecasts (ECMWF) operational wind fields at T799 spectral resolution were used to drive the dispersion model of FLEXPART. The ECMWF modelled data were retrieved with a temporal resolution of 3 h (analyses at 00:00, 06:00, 12:00, and 18:00 UTC; forecasts at 03:00, 09:00, 15:00,

ACPD
15, 22715–22779, 2015

and 21:00 UTC), interpolated to horizontal resolution of 0.2° × 0.2° on the Gaussian grid over Canada and the US (180° W to 0° E and 20 to 90° N) nested in a global grid with resolution of 1° × 1°. Both grids had 91 vertical levels. The FLEXPART Lagrangian particle dispersion model (Stohl et al., 2005) was used to simulate the 5 day transport history (retroplume) of the fossil fuel CO_2 mole fractions at each station location. The model calculated the trajectories of 5000 particles daily at 21:00 UTC (14:00 to 16:00 LST depending on time zones) from the intake height at each station location being considered.

Retroplume spatial distributions were output as 30 min averages on a 0.2° × 0.2° degree grid. The retroplumes were then summed up for the entire 5 days for each time point of particle release. FLEXPART outputs the retroplumes in units of s kg^{-1} m^3, which is the residence time of the plume per grid cell divided by the air density. The footprint layer of the retroplume for FLEXPART is fixed at the standard 100 m layer adjacent to the Earth's surface (Stohl et al., 2005). The modelled fossil fuel CO_2 mole fractions were constructed by multiplying the footprint layer with the monthly prior fossil fuel CO_2 fluxes at 0.2° × 0.2° in kg s^{-1} and summed up over all grid cells (plus the baseline or the contribution from prior to the 5 day simulation period, described below) to yield the time series of modelled fossil fuel CO_2 mole fractions at the measurement station (Stohl et al., 2003, 2009; Cooper et al., 2010).

2.4 Baseline estimations

The station-specific baseline in this context is considered the influence from outside the continent far from the inversion domain. The mole fractions of the fossil fuel CO_2 were sampled from the CT2011 predicted global fossil fuel CO_2 field at the positions (latitude, longitude and altitude) of 5000 particles at the end of the 5th day backward simulation for each station released at 21:00 UTC daily to obtain 5000 mole fraction values. These 5000 mole fractions were averaged to represent the mean baseline for each release time point. The station-specific baseline time series was subsequently subtracted from the synthetic observations that were sampled from CT2011 for each

ACPD
15, 22715–22779, 2015

station. This allowed us to infer fluxes over the region of interest. Errors in the baseline estimation in this study were treated as a part of the transport error when CT2011 mole fractions were used as the "target".

2.5 Two Bayesian inversion methods

In addition to the more commonly known CFM approach, we include a simulation-based method for parameter estimations, MCMC. The performances of the two inversion methods in terms of percentage differences between the posterior estimates and the target fossil fuel CO_2 fluxes are assessed. Note that matrices and vectors are in bold and italic throughout this paper, whereas scalar quantities are in italic font. Inversion was done separately for the western and eastern domains, and for each month of 2009.

2.6 Simulation-based Markov-Chain Monte Carlo (MCMC) Method

The prior gridded fluxes of fossil fuel CO_2, $\{x_{g,p,t}\}$ were re-distributed from the original $1^\circ \times 1^\circ$ uniformly to the same spatial resolution of $0.2^\circ \times 0.2^\circ$ as the emission source sensitivities (or footprints), $\{M_{g,p,t,s}\}$ where the subscripts are, g for a given grid cell in space, sub-region p, station s and time t. $x_{g,p,t}$ is the gridded emission field over sub-region p at time t. The footprints vary in space, time and stations. The modelled mole fractions in our experiments were limited to 21:00 UTC daily (14:00 to 16:00 LST depending on time zones) in January through December for 2009 to avoid temporal correlation and night time processes. Two regions of interest are the two neighboring provinces of Alberta and Saskatchewan (western region), and separately, the province of Ontario (eastern region) in Canada. Any remaining contributions from outside of the inversion region but within the 5 day integration period were subtracted from the synthetic observations for each station in addition to the station-specific baseline time series.

ACPD
15, 22715–22779, 2015

Using a simple linear regression model (likelihood function), linear scaling factors λ_p for $x_{g,p,t}$ are estimated to fit the synthetic observations $y_{t,s}$. The potential advantage of this linear regression model is that fewer assumptions are needed compared to the typical CFM method (Sect. 2.7). This simple regression method is compared to the CFM method to evaluate these two approaches. The regression model is shown below:

$$y_{t,s} = \sum_{p \in R} \lambda_p \sum_{g \in G} M_{g,p,t,s} x_{g,p,t} + \epsilon_{t,s} \quad (1)$$

for station s, at time t, scaling factors λ_p for sub-region p to be estimated, $M_{g,p,t,s}$ is the station-specific emission sensitivity (footprint) to be summed up over the sub-region p for each FLEXPART footprint grid cell g with G being the total number of grid cells of sub-region p. For a given time t and station s, summing contributions from all sub-regions to the total number of R sub-regions gives the total modelled mole fraction. Let $K_{p,t,s} = \sum_{g \in G} M_{g,p,t,s} x_{g,p,t}$ be the contribution from sub-region p, for station s at time t. We obtain:

$$y_{t,s} = \sum_{p \in R} \lambda_p K_{p,t,s} + \epsilon_{t,s} \quad (2)$$

In the MCMC simulation method, same prior error variances $(\sigma_{\text{prior}})^2$ and $(\sigma_e)^2$ for $\boldsymbol{\lambda}$ ($R \times 1$ vector) and $\boldsymbol{\epsilon}$ ($N \times 1$ vector, where N equal to the total number of synthetic observations which equal to the number of time points times the number of stations) are used as in the CFM method, but the posterior estimates and the uncertainties for $\boldsymbol{\lambda}$ are calculated by drawing samples from the joint distributions of the log likelihood and the assumed distributions of prior parameters $\boldsymbol{\lambda}_{\text{prior}}$ (briefly described below) instead of solving for the parameters analytically. See the detailed description in the Appendix.

To implement the regression model Eq. (1), we consider the following Bayesian inversion settings for the western region and the eastern region. Assume λ_p follows normal distribution with a mean of 1 and a variance of 1 for $(\sigma_{\text{prior}})^2$, which corresponds to

ACPD
15, 22715–22779, 2015

100 % error. In the MCMC method, $(\sigma_e)^2$ is assumed to follow inverse-gamma distribution, the mean and variance for $(\sigma_e)^2$ are prescribed by setting the shape and scale parameters to 2.1 and 1.1 respectively. This gives a mean of 1 and a variance of 10. Sensitivity analysis is performed in the synthetic data experiments (E1, E2 and E4), in which the shape and scale parameters (Appendix) are changed to 2.001 and 1.001 respectively. This gives a mean of 1 and a variance of 1000 for the $(\sigma_e)^2$, which correspond to conjugate non-informative priors. Using non-informative priors allows MCMC to sample parameter estimates from a wide parameter space (Appendix).

In our MCMC simulation, a random-walk Metropolis algorithm (Appendix) (Roberts, 1996; Liu, 2001) was used to obtain posterior scaling factor estimates for the sub-regions. The λ_p is initialized to 1, and each monthly batch inversion has 110 000 iterations (first 10 000 discarded as burn-in samples), thinning rate is set to every 10th (every 10th drawn vector of scaling factor estimates is kept), the number of simulations saved for subsequent inferences is equal to 10 000 for each month. Although the use of mean posterior estimates should be avoided (Tarantola, 2005), it is necessary here to compare the results using MCMC to those using the CFM method. Subsequently, the monthly posterior provincial total flux estimates are calculated using the mean of 10 000 scaling factors simulated by the MCMC procedure multiplied by the prior fluxes as shown in Eq. (3).

$$
\begin{aligned}
S_{\mathrm{AB}} &= \sum_{p=1}^{R} \lambda_{p,\mathrm{AB}} \chi_{p,\mathrm{AB}} \\
S_{\mathrm{SK}} &= \sum_{p=1}^{R} \lambda_{p,\mathrm{SK}} \chi_{p,\mathrm{SK}} \\
S_{\mathrm{ON}} &= \sum_{p=1}^{R} \lambda_{p,\mathrm{ON}} \chi_{p,\mathrm{ON}}
\end{aligned}
\tag{3}
$$

ACPD
15, 22715–22779, 2015

where S_{AB}, S_{SK} and S_{ON} are the monthly posterior provincial total fossil fuel CO_2 fluxes for Alberta (AB), Saskatchewan (SK), and Ontario (ON) respectively. Note that $\lambda_{p,AB}$, $\lambda_{p,SK}$ and $\lambda_{p,ON}$ are the mean scaling factors of the sub-regions within the respective province simulated by the MCMC method. $\chi_{p,AB}$, $\chi_{p,SK}$ and $\chi_{p,ON}$ are the monthly prior fluxes for sub-region p in the respective province. With large number of simulated scaling factors, various statistics on the posterior provincial total fluxes can be calculated such as the percentiles, standard deviations and 95 % confidence intervals.

2.7 Cost function minimization (CFM) method

The optimal posterior estimates of scaling factors are obtained by minimizing the cost function J,

$$J(\boldsymbol{\lambda}) = (\boldsymbol{y} - \mathbf{K}\boldsymbol{\lambda})^{\mathrm{T}}\mathbf{D}_{\epsilon}^{-1}(\boldsymbol{y} - \mathbf{K}\boldsymbol{\lambda}) + (\boldsymbol{\lambda} - \boldsymbol{\lambda}_{\mathrm{prior}})^{\mathrm{T}}\mathbf{D}_{\mathrm{prior}}^{-1}(\boldsymbol{\lambda} - \boldsymbol{\lambda}_{\mathrm{prior}}) \quad (4)$$

where $\boldsymbol{y}(N \times 1)$ is the vector of observations (synthetic observations). $\boldsymbol{\lambda}(R \times 1)$ is the vector of the posterior scaling factors to be estimated, N = number of time points times number of stations, $\boldsymbol{\lambda}_{\mathrm{prior}}$ is the vector of the prior scaling factors which are all initialized to 1 for all sub-regions and $\mathbf{K}(N \times R)$ is the matrix of contributions from different sub-regions. $\mathbf{K}$ is the product of two matrices, $\mathbf{M}$ and $\boldsymbol{\chi}$. $\mathbf{M}$ is the modelled transport (or footprints in our case) and $\boldsymbol{\chi}$ is the spatial distribution of the surface emission fluxes. A linear regularization term has been added which is the second term on the right hand side of Eq. (4), a typical setup for undetermined (under-constrained due to lack of observations) problems such as atmospheric flux inversion.

The estimate for $\boldsymbol{\lambda}$ is calculated according to the expression below.

$$\boldsymbol{\lambda} = \left(\mathbf{K}^{\mathrm{T}}\mathbf{D}_{\epsilon}^{-1}\mathbf{K} + \mathbf{D}_{\mathrm{prior}}^{-1}\right)^{-1}\left(\mathbf{K}^{\mathrm{T}}\mathbf{D}_{\epsilon}^{-1}\boldsymbol{y} + \mathbf{D}_{\mathrm{prior}}^{-1}\boldsymbol{\lambda}_{\mathrm{prior}}\right) \quad (5)$$

ACPD
15, 22715–22779, 2015

where

$$\mathbf{D}_{\text{prior}}(R \times R) = \begin{bmatrix} (\sigma_{\text{prior}})^2 & 0 & \dots & 0 \\ 0 & (\sigma_{\text{prior}})^2 & \dots & 0 \\ \vdots & \vdots & \ddots & \vdots \\ 0 & 0 & \dots & (\sigma_{\text{prior}})^2 \end{bmatrix} \quad (6)$$

and

$$\mathbf{D}_{\epsilon}(N \times N) = \begin{bmatrix} (\sigma_{\text{e}})^2 & 0 & \dots & 0 \\ 0 & (\sigma_{\text{e}})^2 & \dots & 0 \\ \vdots & \vdots & \ddots & \vdots \\ 0 & 0 & \dots & (\sigma_{\text{e}})^2 \end{bmatrix} \quad (7)$$

The posterior error variance-covariance, $\sum_{\text{post}}$, for the estimates of λ is calculated according to:

$$\sum_{\text{post}} = \left(\mathbf{K}^{\text{T}}\mathbf{D}_{\epsilon}^{-1}\mathbf{K} + \mathbf{D}_{\text{prior}}^{-1}\right)^{-1} \quad (8)$$

The error covariance matrices are typically not known, consequently $\mathbf{D}_{\epsilon}$ and $\mathbf{D}_{\text{prior}}$ are often assumed to be diagonal matrices as presented in Eqs. (6) and (7), where $\mathbf{D}_{\epsilon}$ is the prior model-observation error diagonal matrix that the diagonal elements are $(\sigma_{\text{e}})^2$ and off-diagonal elements are all zeros. This means that the model-observation mismatch errors are assumed to be uncorrelated. Similarly, $\mathbf{D}_{\text{prior}}$ is the prior scaling factor diagonal matrix where the diagonal elements are $(\sigma_{\text{prior}})^2$ and zeros everywhere else. It means that the contributions from the sub-regions are assumed to be uncorrelated. For further simplification, same individual $(\sigma_{\text{e}})^2$ scalar element is assigned to all measurement stations at all time points. Similarly, same individual $(\sigma_{\text{prior}})^2$ is assigned

ACPD
15, 22715–22779, 2015

to all sub-regions being optimized regardless of the variability and magnitude of the source strength from different sub-regions.

Note that the symbols of the individual elements of $y_{t,s}$, λ_p, $M_{g,p,t,s}$, $\chi_{g,p,t}$, $K_{p,t,s}$ for the MCMC method presented in Eqs. (1) and (2) are consistent with the matrix notations used in Eq. (4) $\boldsymbol{y}$, $\boldsymbol{\lambda}$, $\mathbf{M}$, $\boldsymbol{\chi}$, $\mathbf{K}$ for the CFM method. Inversion was done for each month separately, and western and eastern domains separately. Results will be shown for each month of 2009 as well as the annual total.

2.8 Synthetic data experiments

To have a measure of the ability and limitations of the proposed inversion approaches, five components were examined in this study: (1) the magnitude and spatial distribution of the prior fluxes, (2) modelled transport, (3) number of sub-regions (unknowns to estimate), (4) prior variances of the model-observation error $(\sigma_e)^2$ and of the fluxes $(\sigma_{prior})^2$ and (5) inversion methods to estimate the parameters (scaling factors) for the purpose of assessing the sensitivity introduced by each component.

We conducted a series of inversion experiments presented in Table 3 using different combinations of the five components mentioned previously. The results of the experiments using simulated mole fractions of fossil fuel CO_2 for the year 2009 should reveal whether the provincial annual and monthly total CO_2 fluxes and the spatial distributions could be retrieved by the inversion approaches with an acceptable degree of statistical confidence.

The experiments progress with increasing deviations from the target fluxes/transport, as shown in Table 3. E1–E31 and E32–E62 correspond to the two estimation methods of MCMC and CFM, respectively.

Table 3a shows the first (I) set of experiments E1–E10 and E32–E41 that represent the idealized conditions in which transport model error, baseline error, and flux error do not exist. The differences in these experiments are the number of sub-regions to be optimized and the assumed model-observation mismatch $(\sigma_e)^2$ and flux $(\sigma_{prior})^2$ errors. The prior and the target modelled mole fractions were simulated using the same fluxes

ACPD
15, 22715–22779, 2015

of CT2011 fossil fuel CO_2 folded with the footprints from FLEXPART and therefore, transport model and flux errors do not exist.

To contrast, Table 3b shows the second (II) set of experiments E11–E17 and E42–E48, that the CT2010 fossil fuel CO_2 fluxes were used instead to simulate the prior mole fractions for each station. In this set of experiments, small flux error is introduced (only within the provincial inversion domains, Table 2), but modelled transport remains perfect.

Table 3c shows the third set (III), E18–E24 and E49–E55 that were used to assess the impact of transport model error alone on the estimated fluxes. This is achieved by simulating the prior mole fractions in FLEXPART and sampling the target mole fractions (synthetic observations) modelled by CT2011 with the baseline mole fractions subtracted (see Sect. 2.4). Both FLEXPART and CarbonTracker used the same set of CT2011 monthly fossil fuel CO_2 fluxes.

Lastly, Table 3d shows the fourth (IV) set, E25–E31 and E56–E62 that were used to assess the combined impacts of transport model and flux errors on the estimated fluxes. This is achieved by simulating the prior mole fractions in FLEXPART using the CT2010 monthly fossil fuel CO_2 fluxes and sampling the target mole fractions (synthetic observations) from CT2011 which uses the CT2011 monthly fossil fuel CO_2 fluxes. This set of experiments represents more realistic scenarios in which transport and flux errors exist and the experiments can be considered similar to inversions using real observations, but possibly with smaller errors. Note that the transport model error includes errors in the simulated synoptic variability by the FLEXPART model and in the baseline mole fractions sampled from the CT2011 using the 5th day end-points of the FLEXPART particle locations.

3 Model results

Simulated fossil fuel CO_2 mole fractions by CarbonTracker are compared to that simulated by FLEXPART from January through December in 2009 as shown in Fig. 3

ACPD
15, 22715–22779, 2015

an example of one inversion experiment (E31). The prior and posterior mole fractions are shown in blue and red respectively. The target mole fractions (synthetic observations) simulated by CT2011 are shown in black. Figure 3a and b shows the inversion results using all thirty-seven and forty-nine census divisions (sub-regions) for AB/SK and ON respectively (to be discussed). Note that stations that are closer to local emission sources show a larger offset between the synoptic and baseline contributions, e.g. Downsview station in Ontario. The prior mole fractions tend to be over-predicted during the summer and under-predicted during the winter particularly for stations that are close to high emission sources, for instance, the LLB and EST stations in the province of AB, and the DOW station in the province of ON. The model results in Fig. 3 seem to indicate that locally, the dispersion of FLEXPART near the station may be too weak during the summer (Fig. 3a for AB/SK) but too strong during the winter (Fig. 3b for ON) in comparison to the transport in CarbonTracker.

The summer over prediction and winter under prediction are evident in AB/SK and ON, even though the monthly prior (CT2010) fossil fuel CO_2 fluxes in AB/SK are systematically lower than the target (CT2011), whereas it is the opposite for ON. This is true also for the no flux error case.

The *annual estimation biases of the posterior flux estimates* (hereinafter referred to as posterior errors) for the provinces of AB and SK combined (western region) and ON (eastern region) are shown in Fig. 4a and b respectively. The monthly posterior errors are shown in Fig. 5a and b for the prior flux error and transport model error cases respectively. Positive (negative) biases are shown as squares above (below) the horizontal line at zero. Tables S1–S4 in the Supplement show the posterior errors for the western and eastern regions (leftmost column) from the monthly (January–December), annual (Y2009) target fluxes, and the standard deviation (YSTD) of the monthly posterior errors according to the experimental design presented in Table 3.

ACPD
15, 22715–22779, 2015

3.1 Set (I): no prior flux and transport error

The results from the first (I) set of experiments E1–E10 (MCMC method) and E32–E41 (CFM method) reveal any inherent errors introduced by the MCMC and the CFM methods respectively. This set of experiments represents the idealized conditions in which transport model and flux errors do not exist. Figure 4 (and Tables S1–S4) shows that there is essentially zero percentage difference (red squares) from the target for the western and eastern regions regardless of any number of sub-regions and the magnitude of the assumed error variances for $(\sigma_e)^2$ and $(\sigma_{prior})^2$ when the MCMC simulation method is used. Although not shown, the percentage error tends to be larger for the sub-regions with small fluxes. Thus the inversion seems to sensibly provide better constraint for sub-regions with strong signals at the measurement stations.

Experiments E32–E41 show that the CFM inversion procedure (in its "standard" version) has strong positive posterior errors. As shown in Fig. 4, the posterior error increases (red squares) as the number of sub-regions increases for both western and eastern regions. These posterior errors are the results of the optimisation scheme, as the prior fluxes and modelled transport are "perfect". The optimisation scheme does contain an important approximation, namely the error covariance matrices $\mathbf{D}_\epsilon$ and $\mathbf{D}_{prior}$ being diagonal matrices with the off-diagonal elements set to 0 (Eqs. 6 and 7) as the error covariances (cov_e) and (cov_{prior}) are not generally known. The effect of this approximation and the relative roles of the two error matrices are illustrated in the experiments E32–E41. Note that throughout the experiments E32–E41, the observational constraint error matrix $\mathbf{D}_\epsilon$ has elements ranging from $28 \times S$ by $28 \times S$ to $31 \times S$ by $31 \times S$ (corresponding to the number of daily (afternoon) synthetic observations for each monthly inversion), where S is the number of stations.

In E32 for Ontario (eastern region), with only 1 sub-region and the prior constraint error matrix $\mathbf{D}_{prior}$ is reduced to 1 by 1 with no off diagonal elements (and no prior covariance error), the inversion procedure works (for all 12 months) with negligible error. This indicates that the diagonal matrix approximation for the large matrix $\mathbf{D}_\epsilon$ did not

ACPD
15, 22715–22779, 2015

produce significant posterior errors in the inversion results, and the assumption of no error covariance among the daily (synthetic) observational constraints appears to be reasonable.

However, E32 for Alberta/Saskatchewan (western region) which has 2 sub-regions, the inversion posterior error is 13 % annually. Monthly error can range up to 36 %. The prior constraint error matrix $\mathbf{D}_{\text{prior}}$ is a 2 by 2 matrix with two off-diagonal elements (with the same value by symmetry). The zero assumption for this off-diagonal element resulted in large error in the inversion, indicative of the significant role the prior flux covariance has on the inversion. The result is similar to the 2 sub-regions used in Ontario (eastern region E33), with 18 % posterior error annually.

The relative importance of model-observation constraint and prior flux constraint was examined further in experiments E33–E36 with 4 sub-regions for AB and SK, and 2 sub-regions for ON. E33 applied comparable weighting (100 %, 100 %) to both $(\sigma_e)^2$ and $(\sigma_{\text{prior}})^2$ in the $\mathbf{D}_e$ and $\mathbf{D}_{\text{prior}}$ matrices. E34 (30 %, 30 %) assigned comparable but small uncertainties for the inversion. E35 (100 %, 30 %) assigned stronger constrain to the prior flux, while E36 (30 %, 100 %) assigned stronger constrain to the (synthetic) observations (smaller uncertainty at 30 %).

The results are clear on the relative roles of the error matrices on the inversion results. Percentage posterior errors in the inversion results progressively increased with relative weighting on the prior constraint (E36 to E34 to E35), the annual posterior errors for the western region of AB/SK ranged from 6 % (E36) to 20 % (E34) to 51 % (E35) shown in Fig. 4a (Table S2). The results are similar for the eastern region of ON (7 to 18 to 28 %) as shown in Fig. 4b (Table S4), the same pattern can be seen on the monthly basis. The missing prior sub-region covariance constraint has strong impact on the inversion results. Conversely the missing observational covariance constraint has little impact on the inversion results. Experiment E34 (30 % and 30 % assigned to $(\sigma_e)^2$ and $(\sigma_{\text{prior}})^2$) again shows that it is the relative weighting of the error matrices that is important, as the results are essentially the same as E33 $\left(100\,\%\right.$ and 100 % to $\left.(\sigma_e)^2\right.$

ACPD
15, 22715–22779, 2015

and $(\sigma_{prior})^2$). The 30 % prior uncertainties in E34 are comparable to similar regional inversion studies, e.g. Gerbig et al. (2003), Zhao et al. (2009), etc.

For the CFM inversion, posterior error increases with the number of sub-regions. The rate of increase is dependent on the relative weighting of the prior uncertainties $(\sigma_e)^2$ and $(\sigma_{prior})^2$. Experiments E36, E37, E38, E39, E40 and E41 used 30 % to $(\sigma_e)^2$ and 100 % to $(\sigma_{prior})^2$, with the number of sub-regions for the AB/SK increasing from 4, 7, 11, 19, 27, 37 respectively, and ON from 2, 4, 6, 12, 24, 49 respectively. The reason for this choice of prior variance values, 30 % for $(\sigma_e)^2$ and 100 % for $(\sigma_{prior})^2$ will be explained more clearly following the discussion on the model sensitivity to the number of sub-regions used in the optimisation next.

As shown in Fig. 4a and b, the inversion posterior errors generally increase with the number of sub-regions, with the corresponding increase in the sub-region prior constraint error matrix size (and corresponding increase in the number of off-diagonal matrix elements set to zero). The annual posterior errors are all positive ranging from 6 to 22 % and 7 to 42 % for AB/SK and ON respectively, using the CFM method. For CFM, posterior error increases with the number of sub-regions, rate of increase is dependent on the relative weighting of the prior and observational constraint uncertainties.

These results indicate the CFM optimization procedure itself can have substantial errors on account of the incomplete information in the cost function, easily reaching 22–42 % depending on the inversion setup (sub-region definitions, measurement sites distribution, etc.). This uncertainty component of the inversion has generally been ignored in previous studies. As this uncertainty is mainly a function of the prior constraint component of the cost function, it should be included in the prior error variance $(\sigma_{prior})^2$ for completeness. Therefore, combining this optimization procedure uncertainty with the typical emission inventory uncertainty of ~ 30 % (e.g. Environment Canada, 2012), it appears reasonable to set $(\sigma_{prior})^2$ to 100 % (or greater since all these uncertainties are poorly known) as in this study. These prior uncertainty settings 30 % for $(\sigma_e)^2$ and 100 % for $(\sigma_{prior})^2$ are used in all the remaining sensitivity experiments.

ACPD
15, 22715–22779, 2015

In summary, there appears to be an inherent increasing systematic positive bias in the posterior flux estimates introduced by the inversion method of CFM, as the number of sub-regions increases, whereas, posterior errors do not depend on the number of sub-regions using the MCMC method when flux and transport model errors do not exist.

3.2 Set (II): prior flux error

The second (II) set of experiments E11–E17 (MCMC method with increasing number of sub-regions) and E42–E48 (CFM method) represents conditions in which there is no transport model error, but only flux error exists. The prior flux is CT2010 and the target flux is CT2011, both transported by FLEXPART. Temporally, there are systematic negative biases of the annual (blue squares in Fig. 4) and monthly (Fig. 5a) total flux estimates using the MCMC method, but they are relatively small compared to the difference between CT2010 and CT2011 (Table 2). For instance, the annual total posterior errors are about −8 and −3 % for AB/SK and ON respectively using the most number of sub-regions. There is no linear relationship between the posterior error and the number of sub-regions using MCMC. The results using the seven spatial definitions for MCMC are marginally different. This characteristic of the MCMC inversion suggests that there is a limit to the number of sub-regions (or parameters) the MCMC method can optimize for a given inversion setup and constraining observations, and increasing this number of sub-regions may not improve the results. Synthetic data inversion like the present study is useful for evaluating the inversion setup to ensure that the (near) optimal number of parameters is used.

Unlike the MCMC method as shown in Fig. 4, posterior errors increase as the number of sub-regions increases in the western and eastern regions using the CFM method, similar to the previous case with only optimisation procedure error. Results suggest that the inherent optimisation error may have a dominant effect on the flux estimate even with only prior flux error. The annual and monthly biases change systematically from being negative to positive from 1 sub-region to 49 sub-regions (census divisions) in

ACPD
15, 22715–22779, 2015

ON, similarly for AB/SK. It is interesting to note when the least number of sub-regions is used, the results of CFM and MCMC are quite comparable, but there appears to be seasonality in the monthly estimation errors using CFM as shown on the right column in Fig. 5a. This indicates that estimating many parameters in high-dimensional space is problematic for CFM. Divergent results appear when high-dimensional parameter space is involved in the inversion. Bielger et al. (2011) noted that parameter-estimation problem using minimization method in particular becomes extremely challenging even with relative few parameters to estimate. Although not shown, spatially, the annual patterns of the posterior fluxes obtained from the MCMC and the CFM methods are very similar to those of the targets. Unrealistic negative fluxes do not exist for the provinces of AB/SK and ON with any number sub-regions using either MCMC or CFM method.

3.3 Set (III): transport error

The third (III) set of experiments E18–E24 (MCMC method) and E49–E55 (CFM method) represents conditions in which flux error does not exist, but there is transport model error which includes errors introduced by the simulations of the short term (5 days) transport and the baseline mole fractions (5 days previous) using the FLEXPART model. Similar to the previous set of experiments, it is important to keep in mind that the inherent optimisation procedure error exists. The target is the CT2011 model results at the 7 stations. Both FLEXPART and CarbonTracker models used CT2011 fossil fuel CO_2 emissions as the prior fluxes.

The posterior errors have positive bias for the annual total flux estimates associated with both MCMC and CFM methods shown as green squares in Fig. 4a and b for AB/SK (western region) and ON (eastern region) respectively. The province of ON has relatively large error compared to the combined result of the two provinces in the western region. The annual flux bias does not have a linear relationship with the number of sub-regions (in contrast to the flux error case) using either inversion method. However, using the MCMC method with the largest number of sub-regions (E24), the annual flux estimates, are the least biased with 25 and 21 % for AB/SK and ON respectively. In

ACPD
15, 22715–22779, 2015

addition, the associated standard deviations (YSTD) of the monthly biases for E24 are relatively small for the regions which means that the solution of the flux estimates is relatively stable. This appears to be a desirable result but the estimates of the individual sub-regions become unstable and some sub-regions have large errors.

In the CFM method, the annual estimation bias does not linearly increase as the number of sub-regions increases. This pattern appears to be the combination of the bias introduced by the transport error (similar to the MCMC results) and the increasing positive bias with the number of sub-regions from the optimisation procedure itself (shown in Sect. 3.1). Comparing to the MCMC results, the biases of the annual total flux estimates using the largest number of sub-regions (E55) are 46 and 79 % for AB/SK and ON respectively. However, it is similar to the results using MCMC that the standard deviations (YSTD) of the monthly errors using the most number of sub-regions are relatively small except for AB/SK in which there is no significant difference in the annual errors using different number of sub-regions.

On the monthly time scale for the MCMC results as shown in Fig. 5b, there is a tendency of negative bias during the months of June–August (summer) for the provinces of AB/SK. Negative posterior errors only occur in warmer months of May–July for the province of ON using the MCMC method. The modelled time series of FLEXPART and CT2011 (Fig. 3) indicate that negative flux biases are due to the FLEXPART model over-predicting (compared to CT2011) the mole fractions at most of the stations being considered in the western region during the summer. Over-prediction in the mole fractions of fossil fuel CO_2 subsequently leads to under-estimation (blue cells) in Tables S1–S4 in the posterior fluxes. The reversal behavior of over-estimation (red/orange/yellow cells) in the posterior fluxes occurs during the winter because of the under-prediction in the mole fractions in the cold season. As shown in Fig. 5b, the shape and the amplitude of seasonality of the monthly biases using the CFM method appear to be consistent with the MCMC method. The variability tends to reduce using the most number of sub-regions for both inversion methods.

ACPD
15, 22715–22779, 2015

Spatially, the annual patterns of the posterior fluxes obtained from the MCMC (not shown) and the CFM (not shown) methods appear to be similar to those of the targets. It is similar to set (II) of experiments in that, unrealistic negative fluxes appear in the province of ON using six or more sub-regions when either MCMC (not shown) or CFM (not shown) method is used, whereas negative fluxes do not appear for AB/SK regardless the number of sub-regions.

In summary, when only transport model error exists, the magnitude and variability of biases are relatively large independent of inversion methods compared to the previous set of experiments in which only flux error exists. This suggests that the accuracy of the posterior fluxes is more dependent on the modelled transport than on the prior fluxes in all the experiments we performed. Therefore the relative importance of this effect highlights the need of using the best possible transport model(s) for inversions. In absolute terms, the annual percentage errors are relatively small using the MCMC estimation method in comparison with the CFM estimation method.

3.4 Set (IV): prior flux and transport combined error

The fourth (IV) set of experiments E25–E31 (MCMC method) and E56–E62 (CFM method) represents conditions in which both flux and transport model errors exist. Similar to the third (III) set of experiments, the posterior errors do not systematically decrease as the number of sub-regions increases in the MCMC method in the AB/SK and ON regions. As shown in Fig. 4a and b (black squares), the lack of dependence on the number of sub-regions and the similarity of the non-linear pattern compared to set (III) confirm the fact that the estimation bias are introduced and dominated by the transport model error. Transport model error often confounds inversion results and increases uncertainties. The combined (cancelling) effects of the prior flux and transport model errors are evident in the estimation biases as shown in the figures comparing to the previous two sets of experiments. Although the biases do not linearly depend on the number of sub-regions, in E31 which uses the most number of sub-regions, the biases are 4 and 16 % as shown in Fig. 4a and b for AB/SK and ON respectively which

ACPD
15, 22715–22779, 2015

are the smallest in set E25–E31. To compare, the biases of E62 which has the same setup as E31 are 23 and 73 % for the AB/SK and ON regions when the CFM method is used. Figure 6a and b shows the linear regression analysis using all months of 2009 that plot modelled against synthetic observation fossil fuel CO_2 using all thirty-seven and forty-nine sub-regions for AB/SK and ON respectively. The regression analyses of the prior and posterior CO_2 mole fraction results are shown in blue and red respectively. The improvement of the fit in terms of R^2 and the slope of the regression is the most substantial for the DOW station located in ON, which has the largest synoptic variability among all seven stations. Another indication that this station is the most affected by local fossil fuel CO_2 sources. Note that stations EST in AB and DOW in ON have the lowest R^2. All the inversion cases resulted in better slope and R^2, but the posterior estimate biases as presented in Tables S1–S4 could be larger than the percentage difference of the prior and target fluxes (Table 2) which means the flux estimates are not necessarily better than the prior even with larger R^2. Thus improvements in R^2 in the posterior results are not necessarily a validation of the inversion results.

Figures 7 and 8 show spatially, the annual estimation errors (rightmost column) from the target flux for the seven spatial definitions over the provinces of AB/SK and ON respectively using the MCMC method. Blue and red areas represent under- and over-estimations compared to the target. There is a systematic underestimation (blue areas) using the MCMC method for the most part of AB/SK and ON, particularly for those areas that are far away from the stations and where the prior fluxes are relatively small. In other words, the variability (as a function of the number of sub-regions) of the spatial patterns appears to be limited to those areas where prior fluxes are large and close to the stations. Unrealistic negative posterior fluxes (black sub-regions) appear for the province of ON when six or more sub-regions (E28 to E31) are used which are consistent with previous sets of experiments. We note also that the posterior errors around the stations can be much larger than the percentage differences of the prior and the target fluxes, and there is no improvement with increasing sub-region resolution. This means that the accuracy of the inversion results is not simply determined by the sen-

ACPD
15, 22715–22779, 2015

sitivity of the station's footprints, that high sensitivity does not guarantee reliable flux estimates. The posterior errors around stations are particularly noticeable using the CFM method that is to be discussed next.

Figures 9 and 10 show that the annual spatial patterns obtained from the CFM method are quite consistent with those obtained from the MCMC method, but the errors tend to be more positive possibly due to the inherent positive bias from the optimisation procedure as identified in Sect. 3.1. The posterior errors are not linearly dependent on the number of sub-regions using the CFM method. This might be caused by the non-linear nature of cost function in which the two terms in Eq. (4) are dependent on each other and the confounding impact of the transport error. However, the standard deviations (YSTD) of the monthly posterior errors are the least variable using the most number of sub-regions for both the western and eastern regions. This is consistent with the results using the MCMC method.

Results of a few sub-regions using the CFM estimation method show large monthly variability compared to the relatively small seasonality of the target fluxes (not shown). The spatial patterns of the monthly posterior error appear to be quite sporadic. Similar to the MCMC results, unrealistic negative posterior fluxes (black negative flux sub-regions) as shown in Figs. 9 and 10 appear for the province of ON when six or more sub-regions are used (E59 to E62). These unrealistic sub-regional fluxes are consistent between the two inversion methods and are similar to the transport error only case. It is important to point out again that the spatial patterns of the annual and monthly (not shown) posterior errors increase in similarity using the MCMC and CFM methods as the number of sub-regions decreases. The posterior flux estimates of the two inversion methods in fact become nearly identical when the least number of sub-regions are used. The spatial patterns (Figs. 9 and 10) indicate that the posterior errors do not change using the CFM method for sub-regions that are far away from the stations and in areas where the prior fluxes are relatively small, namely the northwestern AB and northern SK. There is a systematic underestimation (blue areas) using the CFM method for roughly the same sub-regions that are somewhat close to the stations of

ACPD
15, 22715–22779, 2015

EGB and DOW in ON. However, different from the MCMC method, overestimations (red areas) occur in most part of AB/SK and ON that do not change noticeably from month to month (not shown).

In this set of experiments which can be considered to be similar to using real observations as constraint, on the annual time scale, there is a systematic positive bias in the posterior estimates using both MCMC and CFM methods. Note that the biases are relatively small using the MCMC method.

Lastly, we compare quantitatively the posterior flux estimates to the target on monthly and annual time scales. The monthly posterior fluxes and the probability distributions of the annual posterior fluxes in comparison with the targets are shown in Fig. 11 for the three provinces separately. The priors and targets are shown in gray and green for reference. This figure summarizes the results using experiments E28 and E27 as an example in which 11 and 4 sub-regions were used respectively for AB/SK and ON without producing unrealistic negative fluxes. These results are compared to experiment E31 in which all 37 and 49 sub-regions for AB/SK and ON were used respectively. Monthly flux estimates show large intra-annual variability compared to the target (green) fluxes for all three provinces. The annual means are significantly different (all t tests show p values less than 0.0001) between experiments E28 (E27) and E31 for all provinces. As shown in Fig.11a, noticeable error reductions occur in May for AB in which the 5th–95th percentile bands do not overlap. Similarly, there are noticeable error reductions in many months for ON as shown in Fig. 11c. In absolute terms, using the spatial definitions of E31, the means (red vertical lines) of the annual total flux estimates are 136, 36 and 161 Mt for the provinces of AB, SK and ON respectively, which are significantly different from E28 and E27. These results which are relatively less biased in this set of experiments, compare well with the annual target (green vertical lines) fluxes of 130, 36 and 139 Mt for AB, SK and ON respectively. The respective annual posterior errors of E31 for the three provinces are calculated as 5, 0 and 16 %, which compare well with the annual percentage differences of the CT2010 prior and CT2011 target fluxes for AB and SK with −26 and −24 % respectively, but not for ON with 12 %. The worsening

ACPD
15, 22715–22779, 2015

of the flux estimate results compared to the prior for ON is due to the poor modelled transport for some of the stations in this particular province as discussed in Sect. 3.3.

An important feature in Fig. 11 is that the monthly posterior uncertainty estimates (colored bands) could be incorrect (too small) as the uncertainties do not always cover the (sometimes large) differences between the posterior estimates and the target flux values. Another feature evident in Fig. 11 is the fluctuating nature of the inversion results over the limited variations examined in this study. It is clear that inversion results are strongly dependent on the inversion model setup, transport variations with time (different months and seasons) and spatial domain locations, etc. This could be a part of the reason for the widely different posterior flux estimates from different inversion studies with very different setups.

We will continue to investigate how the posterior uncertainty can be improved (more realistic) in our next set of synthetic data experiments examining the impact of different LPDM transport models, different background baseline mole-fraction estimation, observation site selections, etc.

4 Discussions

We have quantitatively assessed our regional inversion system using synthetic observations and target fluxes. In summary, results show that the monthly spatial distributions of the individual sub-regions within the province have large variability (or uncertainty). The annual posterior fluxes over a province appear to have small estimation errors (as a result of the statistical averaging). Another problem when a large number of sub-regions are used for inversion is the appearance of unrealistic (negative) fluxes. However, the optimal number of sub-regions (unknowns) was not fully investigated in this paper and the "optimal" number is likely a function of the prior flux distribution and model transport. The concept of "optimal number" and/or "optimal configuration" would depend on the measure applied. For example, it could depend on the timescale

ACPD
15, 22715–22779, 2015

(monthly, seasonal or annual), the inversion domain (eastern or western Canada), positive definite fluxes and so on.

In this study, the flux signals from outside the inversion domain were not considered explicitly in the optimisation procedure. The FLEXPART model could transport the flux signal from outside the inversion domain over the 5 day integration period differently in comparison to CarbonTracker (another component of the transport error that would contribute to the error of the posterior results). In the next study, it would be useful to test an inversion setup that does optimize the fluxes in this outer region as well as the sensitivity to the estimation of the baseline ("background") mole-fraction value at the beginning of the LPDM integration period (5 days in this study).

There is a consistent pattern across all three provinces and the two inversion methods, but the understanding of flux estimates is complicated for the reason that follows. The posterior error introduced when only the flux error exists (E11–E17 and E42–48) are relatively small compared to those introduced by transport model error (E18–E24 and E49–E55). There is a cancelling effect of the errors when both prior flux and transport model errors exist (E25–E31 and E56–E62) in the regions considered and therefore, this effect is likely a general phenomenon. For the region definitions that lead to realistic (provincial) flux estimates, the numbers of sub-regions for the western region of AB/SK combined and the eastern region of ON are 11 and 4 respectively. The corresponding annual flux estimation errors for the two regions using the MCMC (CFM) method are −7 and −3 % (0 and 8 %) respectively, when there is only prior flux error. The estimation errors increase to 36 and 94 % (40 and 232 %) resulting from transport model error alone. When prior and transport model errors co-exist in the inversions, the estimation errors become 5 and 85 % (29 and 201 %). This result indicates that estimation errors are dominated by the transport model error and can in fact cancel each other and propagate to the flux estimates non-linearly.

Understanding of this combined effect plays an important role toward the intrepretations of the inversion results when real observations are actually used. Although the inversion seems to improve the fit of the synthetic observations using a large number

ACPD
15, 22715–22779, 2015

of sub-regions as shown by the regression plots (Fig. 6), the flux estimates are not necessarily less biased on the annual and provincial scales. In fact, unrealistic results can be expected on the monthly timescale and for some sub-regions.

5 Conclusion

In the development of a regional inversion modelling approach for Canada, this study evaluated various setups and optimisation schemes for regional GHG flux inverse estimation in two different regions in Canada by synthetic-observation inversions. The different sets of experiments progress from no model error to model error comparable to real observation inversion. This approach yielded inversion posterior uncertainties for the different model errors and how these uncertainties interact, as well as finding the suitable model setup for real observation inversion.

Set I is a comparison of two optimisation procedures, MCMC and CFM in the idealised case with no prior flux error or transport error (perfect model). Results show the MCMC method produced the correct posterior fluxes for a range of prior uncertainties, and sub-region distributions. While the CFM method (with the missing prior covariance in the error matrix) is highly sensitive to the prior error variance specified in the prior error matrix and the number of sub-regions used in the inversion (consistent with Bergamaschi et al., 2010). This optimisation procedure error can easily reach 20–40 % depending on the region domain and sub-region resolution in this study. Larger error is possible, as there could be interaction with other errors in the prior fluxes and model transport, etc. Including this large "optimisation procedure error/uncertainty" in the prior flux error variance matrix improved the inversion results. This points to the necessity to account for the optimisation procedure error/uncertainty in any inversion studies.

Prior flux error and perfect model transport experiments (Set II) can help define the near optimal number of sub-regions for the given inversion setup (using the MCMC optimisation in this study), approximately 6–11 sub-regions in the current inversion setups. Inversion based on the near optimal number of sub-regions is helpful for the CFM

ACPD
15, 22715–22779, 2015

method as CFM error can increase with the number of sub-regions being optimised. The CFM posterior errors became increasingly more positive with increasing number of sub-regions, while the MCMC posterior errors approached steady state with increasing number of sub-regions. This suggests the optimisation procedure error (from Set I) and the prior flux error interact weakly in the inversion. Overall MCMC inversion with perfect model transport worked well, the posterior flux errors are reduced by ∼ 75 % in both western and eastern domains.

Correct prior flux with transport error experiments (Set III) showed that the current inversion scheme (adjusting the fluxes only) has (understandably) very limited ability to reduce the model transport errors, large errors of 100–200 % are possible. For the AB/SK domain, MCMC and CFM results are relatively stable with the increasing number of sub-regions, posterior errors varies from 25–50 %. While for the ON domain, MCMC and CFM results are less stable with the number of sub-regions and unrealistic negative fluxes are possible for large number of sub-regions. Posterior errors are highly unstable and can range from 21–98 % (by MCMC) and 79–232 % (by CFM). This suggests the current inversion setup in ON is not suitable for inversion analysis.

The more realistic experiments with both prior flux error and transport error (Set IV) showed similar posterior results as transport error only case (Set III), as the transport error is the largest error in our case studies. The posterior errors are smaller than Set III, as the errors from Set II (prior flux error case tends to be negative) and Set III (transport error case tends to be positive) offset each other. However, the range of variability for the posterior errors is still large, similar to Set III. Again, negative posterior fluxes are possible for large number of sub-regions in ON (AB/SK results appear stable with no negative posterior fluxes), consistent with Set III results.

Overall, MCMC results based on simpler (than CFM) inversion constraint criteria with more complete prior information have smaller posterior errors and more robustness in our sensitivity analysis than the CFM method (consistent with Miller et al., 2014). Synthetic observation inversions provided useful information and identified problems on the different components of prior and posterior errors and uncertainties. There can be

ACPD
15, 22715–22779, 2015

danger in doing inversion without proper evaluation of the inversion model (formulation, sensitivity, robustness, stability, etc.), results could have > 100 % posterior error with unrealistically small posterior uncertainties. In this analysis and evaluation, the AB/SK regional inversion results seem reasonable and stable, and this region appears suitable for real observation inversion.

Appendix

The prior gridded fluxes of fossil fuel CO_2, $\{x_{g,p,t}\}$ were re-distributed to have the same spatial resolution of $0.2^\circ \times 0.2^\circ$ as the emission source sensitivities (or footprints), $\{M_{g,p,s,t}\}$ where index g for a given grid cell in space, sub-region p, station s and time t. $\chi_{g,p,t}$ is the gridded emission field over sub-region p at time t. The linear scaling factors of $\chi_{g,p,t}$ are estimated to fit the synthetic observations $y_{t,s}$ below:

$$y_{t,s} = \sum_{p \in R} \lambda_p \sum_{g \in G} M_{g,p,t,s} \chi_{g,p,t} + \epsilon_{t,s} \quad \text{(A1)}$$

for station s, at time t, scaling factors λ_p for sub-region p to be estimated, $M_{g,p,t,s}$ is the station-specific emission sensitivity (footprint) to be summed up over the sub-region p for each FLEXPART footprint grid cell g with G being the total number of grid cells of a given footprint. For a given time t and station s, summing contributions from all sub-regions to the total number of R sub-regions gives the total modelled mole fraction. To further simplify, let $K_{p,t,s} = \sum_{g \in G} M_{g,p,t,s} \chi_{g,p,t}$ be the contribution from sub-region p, for station s at time t. We obtain:

$$y_{t,s} = \sum_{p \in R} \lambda_p K_{p,t,s} + \epsilon_{t,s} \quad \text{(A2)}$$

where we set the prior $\lambda_p \sim N(1, \sigma^2_{\text{prior}})$, and the so-called model-observation mismatch $\epsilon_{t,s} \sim N(0, \sigma^2_\epsilon)$. The likelihood function $L(\boldsymbol{y}|\boldsymbol{\lambda}, \sigma^2_\epsilon)$ that assumes $\epsilon_{t,s}$ being i.i.d.

ACPD
15, 22715–22779, 2015

becomes:

$$L\left(\boldsymbol{y}|\boldsymbol{\lambda},\sigma_\epsilon^2\right) = \prod_{t=1,s=1}^{N}\left(\frac{1}{2\pi\sigma_\epsilon^2}\right)^{\frac{1}{2}}\exp\left\{\frac{-1}{2\sigma_\epsilon^2}\left(y_{t,s}-\sum_{p\in R}\lambda_p K_{t,s,p}\right)^2\right\} \tag{A3}$$

$$= \left(\frac{1}{2\pi\sigma_\epsilon^2}\right)^{\frac{N}{2}}\exp\left\{\frac{-1}{2\sigma_\epsilon^2}\sum_{t=1,s=1}^{N}\left(y_{t,s}-\sum_{p\in R}\lambda_p K_{t,s,p}\right)^2\right\} \tag{A4}$$

where $N = \sum_{t,s} n_{t,s}$ is the total number of synthetic observations. In matrix form, the likelihood of the synthetic observations $\boldsymbol{y}_{N\times 1}$ is:

$$L\left(\boldsymbol{y}|\boldsymbol{\lambda},\sigma_\epsilon^2\right) = \left(\frac{1}{2\pi\sigma_\epsilon^2}\right)^{\frac{N}{2}}\exp\left\{\frac{-1}{2\sigma_\epsilon^2}(\boldsymbol{y}-\mathbf{K}\boldsymbol{\lambda})^{\mathrm{T}}(\boldsymbol{y}-\mathbf{K}\boldsymbol{\lambda})\right\} \tag{A5}$$

Notice that $\mathbf{K}$ is the matrix with dimension $N \times R$ and $\boldsymbol{\lambda}$ is a R-dimension vector. The non-informative conjugate prior for the variance parameter, σ_ϵ^2, is assumed to follow the inverse-gamma distribution's probability density function with shape parameter α and scale parameter β. The probability density function is:

$$\pi\left(\sigma_\epsilon^2\right) = \frac{\beta^\alpha}{\Gamma(\alpha)}(\sigma_\epsilon^2)^{-\alpha-1}\exp\left(-\frac{\beta}{\sigma_\epsilon^2}\right) \tag{A6}$$

And the scaling factors $\boldsymbol{\lambda}_{R\times 1}$ are assumed to be independent and identically distributed (i.i.d.) following the multivariate normal distribution with mean vector $\boldsymbol{\lambda}_{\text{prior}}$ and covariance matrix $\sigma_{\text{prior}}^2 I_R$ (diagonal matrix). The probability density function for $\boldsymbol{\lambda}$ is:

$$\pi(\boldsymbol{\lambda}) = \left(\frac{1}{2\pi\sigma_{\text{prior}}^2}\right)^{\frac{R}{2}}\exp\left\{\frac{-1}{2\sigma_{\text{prior}}^2}(\boldsymbol{\lambda}-\boldsymbol{\lambda}_{\text{prior}})^{\mathrm{T}}(\boldsymbol{\lambda}-\boldsymbol{\lambda}_{\text{prior}})\right\} \tag{A7}$$

ACPD
15, 22715–22779, 2015

where $\boldsymbol{\lambda}_{\text{prior}}$ is assumed (initialized) to be 1.

Since we assume that all synthetic observations in the data set are independent, according to the Bayes' rule, the joint posterior density is:

$$\pi\left(\boldsymbol{\lambda}, \sigma_\epsilon^2 | \boldsymbol{y}\right) \propto \pi\left(\sigma_\epsilon^2\right) \pi(\boldsymbol{\lambda}) L\left(\boldsymbol{y} | \boldsymbol{\lambda}, \sigma_\epsilon^2\right) \tag{A8}$$

$$\pi\left(\boldsymbol{\lambda}, \sigma_\epsilon^2 | \boldsymbol{y}\right) = k\pi\left(\sigma_\epsilon^2\right) \pi(\boldsymbol{\lambda}) L\left(\boldsymbol{y} | \boldsymbol{\lambda}, \sigma_\epsilon^2\right) \tag{A9}$$

where k is a normalizing constant which is to ensure the cumulative distribution (integral) of the joint posterior density equal to 1. The logarithm of the joint posterior density becomes:

$$\log\left(\pi\left(\boldsymbol{\lambda}, \sigma_\epsilon^2 | \boldsymbol{y}\right)\right) = \log(k) + \log\left(\pi\left(\sigma_\epsilon^2\right)\right) + \log(\pi(\boldsymbol{\lambda})) + \log\left(L\left(\boldsymbol{y} | \boldsymbol{\lambda}, \sigma_\epsilon^2\right)\right) \tag{A10}$$

where $\boldsymbol{\lambda}$ is the vector of scaling factor parameters (regression coefficients). The term $\log(\pi(\sigma_\epsilon^2))$ is the log of the prior probability density for the model-observation mismatch error. The term $\log(\pi(\boldsymbol{\lambda}))$ is the sum of the log of the prior probability densities for the scaling factors. The term $\log(L(\boldsymbol{y}|\boldsymbol{\lambda}, \sigma_\epsilon^2))$ is the log likelihood given the parameters (i.e. the multiple linear regression model used to fit the synthetic observations). It is difficult to analytically solve for the parameters in Eq. (A10). In most cases for Bayesian analyses, therefore, $\boldsymbol{\lambda}$ are sampled from the (complex) joint posterior density using MCMC. The random-walk Metropolis algorithm that is applied in this study is one of the MCMC methods, which is briefly described as follows:

Suppose I samples (number of iterations) are drawn from a multivariate distribution with probability density function $f(\boldsymbol{\lambda}|\boldsymbol{y})$. Suppose $\boldsymbol{\lambda}^i$ is the ith sample from f, where $\boldsymbol{\lambda}^i = (\lambda_1, \lambda_2, \ldots, \lambda_p)^{\mathrm{T}}$ is the transposed vector of scaling factors and p is the number of sub-regions in this study. To use the Metropolis algorithm, an initial value $\boldsymbol{\lambda}^0$ and a multivariate proposal density $q(\boldsymbol{\lambda}^{i+1}|\boldsymbol{\lambda}^i)$ are required. For the $i(+1)$th iteration, the algorithm generates a sample from a $q(.|.)$ based on the current sample $\boldsymbol{\lambda}^i$, and it makes a decision to either accept or reject the new sample. If the new sample is accepted, the

ACPD
15, 22715–22779, 2015

algorithm repeats itself by starting at the new sample. If the new sample is rejected, the algorithm starts at the current point and repeats. Suppose $q(\boldsymbol{\lambda}_{\text{new}}|\boldsymbol{\lambda}^i)$ is a symmetric distribution. The proposal distribution should be a simple (e.g. Gaussian or unimodal) distribution from which to sample, and it must be such that $q(\boldsymbol{\lambda}_{\text{new}}|\boldsymbol{\lambda}^i) = q(\boldsymbol{\lambda}^i|\boldsymbol{\lambda}_{\text{new}})$, meaning that the likelihood of jumping to $\boldsymbol{\lambda}_{\text{new}}$ from $\boldsymbol{\lambda}^i$ is the same as the likelihood of jumping back to $\boldsymbol{\lambda}^i$ from $\boldsymbol{\lambda}_{\text{new}}$. The most common choice of the proposal distribution is the multivariate normal distribution $N(\boldsymbol{\lambda}\boldsymbol{\Sigma})$, with p-dimensional mean vector $\boldsymbol{\lambda}$ and $p \times p$ covariance matrix $\boldsymbol{\Sigma}$. The random-walk Metropolis algorithm can be summarized as follows:

- Set $n = 0$. Choose a starting point λ^0. This can be an arbitrary point as long as $f(\boldsymbol{\lambda}^0|\boldsymbol{y}) > 0$.
- Generate a new sample, $\boldsymbol{\lambda}_{\text{new}}$, by using the proposal distribution $q(.|\boldsymbol{\lambda}^i)$.
- Calculate the following quantity: $r = \min\left\{\frac{f(\boldsymbol{\lambda}_{\text{new}}|\boldsymbol{y})}{f(\boldsymbol{\lambda}^i|\boldsymbol{y})}, 1\right\}$.
- Draw a random sample u from the uniform distribution $U(0,1)$.
- Set $\boldsymbol{\lambda}^{i+1} = \boldsymbol{\lambda}_{\text{new}}$ if $u < r$; otherwise set $\boldsymbol{\lambda}^{i+1} = \boldsymbol{\lambda}^i$.
- Set $i = i + 1$. If $i < I$, the number of desired samples, return to step 2. Otherwise, stop.

This algorithm defines a chain of random variates whose distribution will converge to the desired distribution $f(\boldsymbol{\lambda}|\boldsymbol{y})$, and so from some point forward, the chain of samples is a sample from the distribution of interest. In Markov chain terminology, this distribution is called the stationary distribution of the chain, and in Bayesian statistics, it is the posterior distribution of the model parameters (scaling factors in this study).

For detailed descriptions and proofs in MCMC method and Bayesian analysis, there are articles and books among many including Besag et al. (1995), Chib and Greenberg

ACPD
15, 22715–22779, 2015

(1995), Gilks et al. (1996), Kass et al. (1998) and Congdon (2006). Here we only describe the steps and diagnostics that were used to conduct MCMC simulations for the purpose of parameter estimations in this synthetic flux inversion study. The inversions were done separately for the western and the eastern provinces. The scaling factors λ_p were initialized to 1 with a variance of 1 which was equivalent to setting 100 % uncertainty for the emissions in each sub-region. The variance parameter $(\sigma_e)^2$ can be considered as the total model-observation mismatch (or total model error). This parameter is assumed to have the inverse-gamma distribution. The mean of $(\sigma_e)^2$ is calculated as scale/(shape – 1) when shape is greater than 1 and variance of $(\sigma_e)^2$ is equal to scale^2/[(shape – 1)^2(shape – 2)] when shape is greater than 2. With the shape and scale parameters being set to 2.001 and 1.001, this gives a mean of 1 and variance of 1000 which is similar to setting a large uncertainty for the model-observation mismatch error. This large prescribed uncertainty corresponds to conjugate non-informative prior for the $(\sigma_e)^2$. Conjugate priors are required to ensure the target posterior distribution having a closed form. This total model-observation mistmatch error has been estimated to be about 30 % in previous studies that used the CFM method (Zhao et al., 2009; Gerbig et al., 2003; among others) which included measurement error, transport error, aggregation error and so on.

In previous inverse modelling studies the parameters of interest were assumed to be fixed constants and determined analytically. Instead of treating parameters as fixed constant, we applied Bayesian analysis with MCMC random sampling method that treated parameters as random variables. Often times, these parameters cannot be determined exactly, and particularly the uncertainty about the parameter has no known analytical form in a high-dimensional parameter distribution space. Using MCMC sampling method, our inference was based on the probability distribution for the parameter. In this paper, we did not address the impact of the covariances in the uncertainty matrices, or the magnitude of the assumed prior emission and model uncertainties. Hence, the off-diagonal elements in the covariance matrix were simply set to zeros.

ACPD
15, 22715–22779, 2015

There is no simple way to calculate the uncertainties of the posterior distributions of the scaling factors. In fact an analytical form of the uncertainties is not required in our simulation approach. Within the Bayesian framework, conducting simulation to estimate the uncertainties for parameter of interests becomes straightforward because the posterior distributions of scaling factors (uncertainties about the posterior scaling factors) can be obtained by simulation while taking into account the uncertainties in all the parameters by treating them as random variables (SAS/STAT®, 2013). We performed Bayesian analysis for January through December 2009 for each individual month. The MCMC procedure which uses the random-walk Metropolis algorithm to sample the posterior probability density expressed in Eq. (A10) in which the SAS/STAT® system was used to conduct the simulations.

In total 110 000 samples (scaling factor estimates) were drawn by MCMC simulations for each month in year 2009. 10 000 burn-in samples were used to minimize the effect of the initial values (all scaling factors were initialized to 1) on the posterior inference, that is, the initial 10 000 drawn MCMC samples were discarded. A thinning rate of 10 was used to reduce sample autocorrelations. Although 110 000 iterations were conducted, only every 10th sample was kept for subsequent inferences for the posterior flux estimates to minimize autocorrelation. All diagnostic trace plots (not shown) for all the parameters (scaling factors) showed good mixing (fast convergence), that was, the efficiency that the posterior parameter space was explored by the Markov chain. This was a good indication of the sub-regions that were not strongly correlated in space due to similar transport. Hence, there was no serious multi-linearity problem of the parameters in the regression model (likelihood function). It also means that the Markov chain quickly traversed the support of the distribution to explore both the tails and the mode areas efficiently and the parameters reached their stationary distributions. Geweke diagnostics showed constant mean and variance of the Markov Chain. Heidelberger and Welch diagnostics showed stationarity of the Markov chain. Raftery and Lewis diagnostics showed the number of iterations was sufficient to estimate the percentiles of the parameters. The effective sample size calculated also showed that

ACPD
15, 22715–22779, 2015

the number of iterations used was sufficient for inferences. The Monte Carlo standard errors of the mean estimates for each of the parameters were small, with respect to the posterior standard deviations. This means that only a fraction (less than 1 %) of the posterior variability was due to the simulation.

In all but the simplest cases of inversions that have low dimensions (i.e. only a few parameters), it is not possible to estimate parameters from a complicated joint posterior distribution directly and analytically. Often, Bayesian methods rely on simulations to generate samples from the desired posterior distribution and use the simulated draws to approximate the distribution and to make statistical inferences, and this is carried out in this study for comparison. Note that however, the definition of central estimators such as the mean or the median and of estimators of uncertainty such as the error variance-covariance matrix fail to have any useful representativeness in a high-dimensional problem in which the posterior distributions of the parameters can actually be multi-modal. Therefore, the use of the common practice of reporting the means or medians posterior estimates should be abandoned, even if the results are accompanied by some analysis of error (Tarantola, 2005).

The Supplement related to this article is available online at doi:10.5194/acpd-15-22715-2015-supplement.

Acknowledgement. We thank Owen R. Cooper for providing valuable support for setting up the FLEXPART model and NOAA ESRL for making the global surface fluxes and 3-D CO_2 mole fraction fields from CarbonTracker publicly available.

ACPD
15, 22715–22779, 2015

References

Andres, R. J., Gregg, J. S., Losey, L., Marland, G., and Boden, T. A.: Monthly, global emissions of carbon dioxide from fossil fuel consumption, Tellus B, 63, 309–327, doi:10.1111/j.1600-0889.2011.00530.x, 2011.

Bergamaschi, P., Krol, M., Dentener, F., Vermeulen, A., Meinhardt, F., Graul, R., Ramonet, M., Peters, W., and Dlugokencky, E. J.: Inverse modelling of national and European CH_4 emissions using the atmospheric zoom model TM5, Atmos. Chem. Phys., 5, 2431–2460, doi:10.5194/acp-5-2431-2005, 2005.

Bergamaschi, P., Krol, M., Meirink, J. F., Dentener, F., Segers, A., van Aardenne, J., Monni, S., Vermeulen, A., Schmidt, M., Ramonet, M., Yver, C., Meinhardt, F., Nisbet, E. G., Fisher, R., O'Doherty, S., and Dlugokencky, E. J.: Inverse modeling of European CH_4 emissions 2001–2006, J. Geophys. Res., 115, D22309, doi:10.1029/2010JD014180, 2010.

Besag, J., Green, P., Higdon, D., and Mengersen, K.: Bayesian computation and stochastic systems, Stat. Sci. 10, 3–66, 1995.

Biegler, L., Biros, G., Ghattas, O., Heinkenschloss, M., Keyes, D., Mallick, B., Marzouk, Y., Tenorio, L., Waanders, B. V. B., and Willcox, K.: Large-Scale Inverse Problems and Quantification of Uncertainty, Computational Statistics, John Wiley & Sons Ltd, UK, 2011.

Boden, T. A., Marland, G. and Andres, R. J.: Global, Regional, and National Fossil-Fuel CO_2 Emissions. Carbon Dioxide Information Analysis Center, Oak Ridge National Laboratory, U.S. Department of Energy, Oak Ridge, Tenn., USA, doi:10.3334/CDIAC/00001_V2013, 2013.

Brioude, J., Kim, S.-W., Angevine, W. M., Frost, G. J., Lee, S.-H., McKeen, S. A., Trainer, M., Fehsenfeld, F. C., Holloway, J. S., Ryerson, T. B., Williams, E. J., Petron, G., and Fast, J. D.: Top-down estimate of anthropogenic emission inventories and their interannual variability in Houston using a mesoscale inverse modeling technique, J. Geophys. Res., 116, D20305, doi:10.1029/2011JD016215, 2011.

Brioude, J., Petron, G., Frost, G. J., Ahmadov, R., Angevine, W. M., Hsie, E.-Y., Kim, S.-W., Lee, S.-H., McKeen, S. A., Trainer, M., Fehsenfeld, F. C., Holloway, J. S., Peischl, J., Ryerson, T. B., and Gurney, K. R.: A new inversion method to calculate emission inventories without a prior at mesoscale: application to the anthropogenic CO_2 emission from Houston, Texas, J. Geophys. Res., 117, D05312, doi:10.1029/2011JD016918, 2012.

Brioude, J., Angevine, W. M., Ahmadov, R., Kim, S.-W., Evan, S., McKeen, S. A., Hsie, E.-Y., Frost, G. J., Neuman, J. A., Pollack, I. B., Peischl, J., Ryerson, T. B., Holloway, J., Brown,

ACPD
15, 22715–22779, 2015

S. S., Nowak, J. B., Roberts, J. M., Wofsy, S. C., Santoni, G. W., Oda, T., and Trainer, M.: Top-down estimate of surface flux in the Los Angeles Basin using a mesoscale inverse modeling technique: assessing anthropogenic emissions of CO, NO_x and CO_2 and their impacts, Atmos. Chem. Phys., 13, 3661–3677, doi:10.5194/acp-13-3661-2013, 2013.

Bruhwiler, L., Dlugokencky, E., Masarie, K., Ishizawa, M., Andrews, A., Miller, J., Sweeney, C., Tans, P., and Worthy, D.: CarbonTracker-CH_4 (2014), an assimilation system for estimating emissions of atmospheric methane, Atmos. Chem. Phys., 14, 8269–8293, doi:10.5194/acp-14-8269-2014, 2014.

CarbonTracker: CT2011 results provided by NOAA ESRL, Boulder, Colorado, USA, available at: http://carbontracker.noaa.gov (last access: 25 November 2013), 2010, 2011.

Chib, S. and Greenberg, E.: Understanding the Metropolis–Hastings algorithm, Am. Stat., 49, 327–335, 1995.

Congdon, P.: Bayesian Statistical Modeling, 2nd edn., John Wiley & Sons, New York, USA, 2006.

Cooper, O. R., Parrish, D. D., Stohl, A., Trainer, M., Nedelec, P., and Thouret, V.: Increasing springtime ozone mixing ratios in the free troposphere over western North America, Nature, 463, 344–348, 2010.

Cressot, C., Chevallier, F., Bousquet, P., Crevoisier, C., Dlugokencky, E. J., Fortems-Cheiney, A., Frankenberg, C., Parker, R., Pison, I., Scheepmaker, R. A., Montzka, S. A., Krummel, P. B., Steele, L. P., and Langenfelds, R. L.: On the consistency between global and regional methane emissions inferred from SCIAMACHY, TANSO-FTS, IASI and surface measurements, Atmos. Chem. Phys., 14, 577–592, doi:10.5194/acp-14-577-2014, 2014.

Enting, I. G., Francey, R. J., Trudinger, C. M., and Granek, H.: Synthesis Inversion of Atmospheric CO_2 Using the GISS Tracer Transport Model, Tech. Rep. Technical Paper no. 29, CSIRO Division of Atmospheric Research, Commonwealth Scientific and Industrial Research Organization, Atmos. Res., Australia, 1993.

Enting, I. G., Trudinger, C. M., and Francey, R. J.: A synthesis inversion of the concentration and δ^{13}C of atmospheric CO_2, Tellus, 47B, 35–52, 1995.

Environment Canada, National Inventory Report 1990–2012: Greenhouse Gas Sources and Sinks in Canada, available at: http://www.ec.gc.ca/ges-ghg/default.asp?lang=En&n=83A34A7A-1 (last access: 15 January 2015), 2012.

ACPD
15, 22715–22779, 2015

Fan, S., Gloor, M., Mahlman, J., Pacala, S., Sarmiento, J., Takahashi, T., and Tans, P.: A large terrestrial carbon sink in North America implied by atmospheric and oceanic CO_2 data and models, Science, 282, 442–446, 1998.

Fan, S.-W., Gloor, M., Mahlman, J., Pacala, S. W., Sarmiento, J. L., Takahashi, T., and Tans, P.: On the use of regularization techniques in the inverse modeling of atmospheric carbon dioxide, J. Geophys. Res., 104, 21503–21512, doi:10.1029/1999JD900215, 1999.

Gerbig, C., Lin, J. C., Wofsy, S. C., Daube, B. C., Andrews, A. E., Stephens, B. B., Bakwin, P. S., and Grainger, C. A.: Toward constraining regional-scale fluxes of CO_2 with atmospheric observations over a continent: 1. Observed spatial variability from airborne platforms, J. Geophys. Res., 108, 4756, doi:10.1029/2002JD003018, 2003.

Gilks, W. R., Richardson, S., and Spiegelhalter, D. J.: Markov Chain Monte Carlo in Practice, Chapman & Hall, London, UK, 1996.

Gloor, M., Bakwin, P., Hurst, D., Lock, L., Draxler, R., and Tans, P.: What is the concentration footprint of a tall tower?, J. Geophys. Res., 106, 17831–17840, doi:10.1029/2001JD900021, 2001.

Jeong, S., Zhao, C., Andrews, A. E., Bianco, L., Wilczak, J. M., and Fischer, M. L.: Seasonal variation of CH_4 emissions from central California, J. Geophys. Res., 117, D11306, doi:10.1029/2011JD016896, 2012.

Kass, R. E., Carlin, B. P., Gelman, A., and Neal, R. M.: Markov Chain Monte Carlo in practice: a roundtable discussion, Stat. Sci., 52, 93–100, 1998.

Kort, E. A., Eluszkiewicz, J., Stephens, B. B., Miller, J. B., Gerbig, C., Nehrkorn, T., Daube, B. C., Kaplan, J. O., Houweling, S., and Wofsy, S. C.: Emissions of CH_4 and N_2O over the United States and Canada based on a receptor-oriented modeling framework and COBRA-NA atmospheric observations, Geophys. Res. Lett., 35, L18808, doi:10.1029/2008GL034031, 2008.

Liu, J. S.: Monte Carlo Strategies in Scientific Computing, Springer, New York, USA, 2001.

Manning, A. J., Ryall, D. B., Derwent, R. G., Simmonds, P. G., and O'Doherty, S.: Estimating UK methane and nitrous oxide emissions from 1990 to 2007 using an inversion modelling approach, J. Geophys. Res. 116, D02305, doi:10.1029/2010JD014763, 2011.

Miller, S. M., Wofsy, S. C., Michalak, A. M., Kort, E. A., Andrews, A. E., Biraud, S. C., Dlugokencky, E. J., Eluszkiewicz, J., Fischer, M. L., Janssens-Maenhout, G., Miller, B. R., Miller, J. B., Montzka, S. A., Nehrkorn, T., and Sweeney, C.: Anthropogenic emissions of methane

ACPD
15, 22715–22779, 2015

in the United States, P. Natl. Acad. Sci., 110, 20018–20022, doi:10.1073/pnas.1314392110, 2013.

Miller, S. M., Michalak, A. M., and Levi, P. J.: Atmospheric inverse modeling with known physical bounds: an example from trace gas emissions, Geosci. Model Dev., 7, 303–315, doi:10.5194/gmd-7-303-2014, 2014.

Oda, T. and Maksyutov, S.: A very high-resolution (1 km × 1 km) global fossil fuel CO_2 emission inventory derived using a point source database and satellite observations of nighttime lights, Atmos. Chem. Phys., 11, 543–556, doi:10.5194/acp-11-543-2011, 2011.

Rigby, M., Manning, A. J., and Prinn, R. G.: Inversion of long-lived trace gas emissions using combined Eulerian and Lagrangian chemical transport models, Atmos. Chem. Phys., 11, 9887–9898, doi:10.5194/acp-11-9887-2011, 2011.

Roberts, G. O.: Markov chain concepts related to sampling algorithms, in: Markov Chain Monte Carlo in Practice, edited by: Gilks, W. R. Spiegelhalter, D. J. and Richardson, S., Chapman & Hall, London, UK, 45–58, 1996.

Rodgers, C. D.: Inverse Methods for Atmospheric Sounding: Theory and Practice, World Scientific Publishing Co. Ltd, Singapore, 2000.

SAS Institute Inc.: SAS/STAT® 13.2 User's Guide, 2nd edn., SAS Institute Inc., Cary, NC, USA, 2013.

Stohl, A., Forster, C., Eckhardt, S., Spichtinger, N., Huntrieser, H., Heland, J., Schlager, H., Aufmhoff, H., Arnold, F., and Cooper, O. R.: A backward modeling study of intercontinental pollution transport using aircraft measurements, J. Geophys. Res., 108, 4370, doi:10.1029/2002JD002862, 2003.

Stohl, A., Forster, C., Frank, A., Seibert, P., and Wotawa, G.: Technical note: The Lagrangian particle dispersion model FLEXPART version 6.2, Atmos. Chem. Phys., 5, 2461–2474, doi:10.5194/acp-5-2461-2005, 2005.

Stohl, A., Seibert, P., Arduini, J., Eckhardt, S., Fraser, P., Greally, B. R., Lunder, C., Maione, M., Mühle, J., O'Doherty, S., Prinn, R. G., Reimann, S., Saito, T., Schmidbauer, N., Simmonds, P. G., Vollmer, M. K., Weiss, R. F., and Yokouchi, Y.: An analytical inversion method for determining regional and global emissions of greenhouse gases: sensitivity studies and application to halocarbons, Atmos. Chem. Phys., 9, 1597–1620, doi:10.5194/acp-9-1597-2009, 2009.

Tarantola, A.: Inverse problem theory and methods for model parameter estimation, SIAM, Philadelphia, PA, USA, 2005.

ACPD
15, 22715–22779, 2015

Thompson, R. L., Gerbig, C., and Rödenbeck, C.: A Bayesian inversion estimate of N_2O emissions for western and central Europe and the assessment of aggregation errors, Atmos. Chem. Phys., 11, 3443–3458, doi:10.5194/acp-11-3443-2011, 2011.

Tolk, L. F., Dolman, A. J., Meesters, A. G. C. A., and Peters, W.: A comparison of different inverse carbon flux estimation approaches for application on a regional domain, Atmos. Chem. Phys., 11, 10349–10365, doi:10.5194/acp-11-10349-2011, 2011

Vogel, F. R., Ishizawa, M., Chan, E., Chan, D., Hammer, S., Levin, I. and Worthy, D. E. J.: Regional non-CO_2 greenhouse gas fluxes inferred from atmospheric measurements in Ontario, Canada. J. Integr. Environ. Sci. 9, 41–55. doi:10.1080/1943815X.2012.691884, 2012.

Zhao, C., Andrews, A. E., Bianco, L., Eluszkiewicz, J., Hirsch, A., MacDonald, C., Nehrkorn, T., and Fischer, M. L.: Atmospheric inverse estimates of methane emissions from Central California, J. Geophys. Res., 114, D16302, doi:10.1029/2008JD011671, 2009.

ACPD
15, 22715–22779, 2015

Table 1. Ground-based in-situ GHG measurement stations and brief descriptions for the surrounding areas.

Station Name, Province	Latitude, Longitude	Elevation (a.s.l., m)	Intake Height (a.g.l., m)	Brief Description
Lac La Biche (LLB), AB	54° 57′N, 112° 27′W	540	10 (50 starting in June 2009)	Wetland region
Esther (EST), AB	51° 40′N, 110° 12′W	707	3m (50m tower started on 7 March 2011)	Rural prairies
East Trout Lake (ETL), SK	54° 21′N, 104° 59′W	493	105	Southern boreal forest of Canada
Bratt's Lake (BRA), SK	51° 12′N, 104° 42′W	595	35	Rural prairies
Fraserdale (FRD), ON	49° 53′N, 81° 34′W	210	40	Between south of the Hudson Bay Lowland and boreal forest region
Egbert (EGB), ON	44° 14′N, 79° 47′W	251	3 (25 starting in Mar 2009)	Rural
Downsview (DOW), ON	43° 47′N, 79° 28′W	198	20	Suburban

ACPD
15, 22715–22779, 2015

Table 2. Provincial monthly (Mt/month) and annual (Mt/year) total fossil fuel CO_2 fluxes from CT2010 and CT2011. The relative percentage differences are calculated for the monthly and annual provincial total between CT2010 and CT2011, i.e. (CT2010 − CT2011)/CT2011 × 100 %.

Release	Prov.	Jan	Feb	Mar	Apr	May	Jun	Jul	Aug	Sep	Oct	Nov	Dec	Y2009
CT2010	AB	9.5	8.7	8.3	7.9	7.3	7.6	8.1	7.9	7.5	7.4	7.8	8.9	96.9
CT2010	SK	2.7	2.5	2.4	2.2	2.1	2.2	2.3	2.2	2.1	2.1	2.2	2.5	27.5
CT2010	ON	15.3	14	13.4	12.8	11.8	12.2	13.1	12.7	12.1	11.9	12.6	14.3	156.2
CT2011	AB	12.7	12.3	11.4	10.5	9.8	9.8	10.1	10.2	10	10.3	11.1	12.1	130.3
CT2011	SK	3.5	3.4	3.1	2.9	2.7	2.7	2.8	2.8	2.8	2.9	3.1	3.3	36
CT2011	ON	13.4	12.8	12	11.3	10.6	10.8	11.2	11.1	10.8	10.9	11.7	12.8	139.4
	AB	−25	−29	−27	−25	−26	−22	−20	−23	−25	−28	−30	−26	−26
$\left(\frac{\text{CT2010}-\text{CT2011}}{\text{CT2011}}\right)$	SK	−23	−26	−23	−24	−22	−19	−18	−21	−25	−28	−29	−24	−24
×100 %	ON	14	9	12	13	11	13	17	14	12	9	8	12	12

ACPD
15, 22715–22779, 2015

Table 3. Synthetic flux inversion experiments. Four sets of experiments are investigated that have small to large errors starting from (I) no prior flux and transport error, (II) prior flux error only, (III) transport error only, and (IV) prior flux and transport error. Common to all (prior modelled transport: FLEXPART, target flux: fossil fuel CO_2 CT2011). Baselines that were sampled from the CT2011 predicted fossil fuel concentration field were required for experiments E18–E31 and E49–E62. Two inversion methods were used for comparison, the Markov-Chain Monte Carlo (MCMC) simulation and cost function minimization (CFM) methods.

(a)

Experiment	Inversion method	Number of sub-regions	$(\sigma_e)^2$, $(\sigma_{prior})^2$ in %	Prior flux	Synthetic obs simulated by
E1/E32	MCMC/CFM	AB/SK:2, ON:1	100, 100	CT2011	CT2011 flux in FLEXPART
E2/E33	MCMC/CFM	AB/SK:4, ON:2	100, 100	CT2011	CT2011 flux in FLEXPART
E3/E34	MCMC/CFM	AB/SK:4, ON:2	30, 30	CT2011	CT2011 flux in FLEXPART
E4/E35	MCMC/CFM	AB/SK:4, ON:2	100, 30	CT2011	CT2011 flux in FLEXPART
E5/E36	MCMC/CFM	AB/SK:4, ON:2	30, 100	CT2011	CT2011 flux in FLEXPART
E6/E37	MCMC/CFM	AB/SK:7, ON:4	30, 100	CT2011	CT2011 flux in FLEXPART
E7/E38	MCMC/CFM	AB/SK:11, ON:6	30, 100	CT2011	CT2011 flux in FLEXPART
E8/E39	MCMC/CFM	AB/SK:19, ON:12	30, 100	CT2011	CT2011 flux in FLEXPART
E9/E40	MCMC/CFM	AB/SK:27, ON:24	30, 100	CT2011	CT2011 flux in FLEXPART
E10/E41	MCMC/CFM	AB/SK:37, ON:49	30, 100	CT2011	CT2011 flux in FLEXPART

ACPD
15, 22715–22779, 2015

Table 3. Continued.

(b)					
Experiment	Inversion method	Number of sub-regions	$(\sigma_e)^2$, $(\sigma_{prior})^2$ in %	Prior flux	Synthetic obs simulated by
E11/E42	MCMC/CFM	AB/SK:2, ON:1	30, 100	CT2010	CT2011 flux in FLEXPART
E12/E43	MCMC/CFM	AB/SK:4, ON:2	30, 100	CT2010	CT2011 flux in FLEXPART
E13/E44	MCMC/CFM	AB/SK:7, ON:4	30, 100	CT2010	CT2011 flux in FLEXPART
E14/E45	MCMC/CFM	AB/SK:11, ON:6	30, 100	CT2010	CT2011 flux in FLEXPART
E15/E46	MCMC/CFM	AB/SK:19, ON:12	30, 100	CT2010	CT2011 flux in FLEXPART
E16/E47	MCMC/CFM	AB/SK:27, ON:24	30, 100	CT2010	CT2011 flux in FLEXPART
E17/E48	MCMC/CFM	AB/SK:37, ON:49	30, 100	CT2010	CT2011 flux in FLEXPART

ACPD
15, 22715–22779, 2015

Table 3. Continued.

(c)					
Experiment	Inversion method	Number of sub-regions	$(\sigma_e)^2$, $(\sigma_{prior})^2$ in %	Prior flux	Synthetic obs simulated by
E18/E49	MCMC/CFM	AB/SK:2, ON:1	30, 100	CT2011	CT2011 flux in CT2011
E19/E50	MCMC/CFM	AB/SK:4, ON:2	30, 100	CT2011	CT2011 flux in CT2011
E20/E51	MCMC/CFM	AB/SK:7, ON:4	30, 100	CT2011	CT2011 flux in CT2011
E21/E52	MCMC/CFM	AB/SK:11, ON:6	30, 100	CT2011	CT2011 flux in CT2011
E22/E53	MCMC/CFM	AB/SK:19, ON:12	30, 100	CT2011	CT2011 flux in CT2011
E23/E54	MCMC/CFM	AB/SK:27, ON:24	30, 100	CT2011	CT2011 flux in CT2011
E24/E55	MCMC/CFM	AB/SK:37, ON:49	30, 100	CT2011	CT2011 flux in CT2011

ACPD
15, 22715–22779, 2015

Table 3. Continued.

(d)

Experiment	Inversion method	Number of sub-regions	$(\sigma_e)^2$, $(\sigma_{prior})^2$ in %	Prior flux	Synthetic obs simulated by
E25/E56	MCMC/CFM	AB/SK:2, ON:1	30, 100	CT2010	CT2011 flux in CT2011
E26/E57	MCMC/CFM	AB/SK:4, ON:2	30, 100	CT2010	CT2011 flux in CT2011
E27/E58	MCMC/CFM	AB/SK:7, ON:4	30, 100	CT2010	CT2011 flux in CT2011
E28/E59	MCMC/CFM	AB/SK:11, ON:6	30, 100	CT2010	CT2011 flux in CT2011
E29/E60	MCMC/CFM	AB/SK:19, ON:12	30, 100	CT2010	CT2011 flux in CT2011
E30/E61	MCMC/CFM	AB/SK:27, ON:24	30, 100	CT2010	CT2011 flux in CT2011
E31/E62	MCMC/CFM	AB/SK:37, ON:49	30, 100	CT2010	CT2011 flux in CT2011

ACPD
15, 22715–22779, 2015

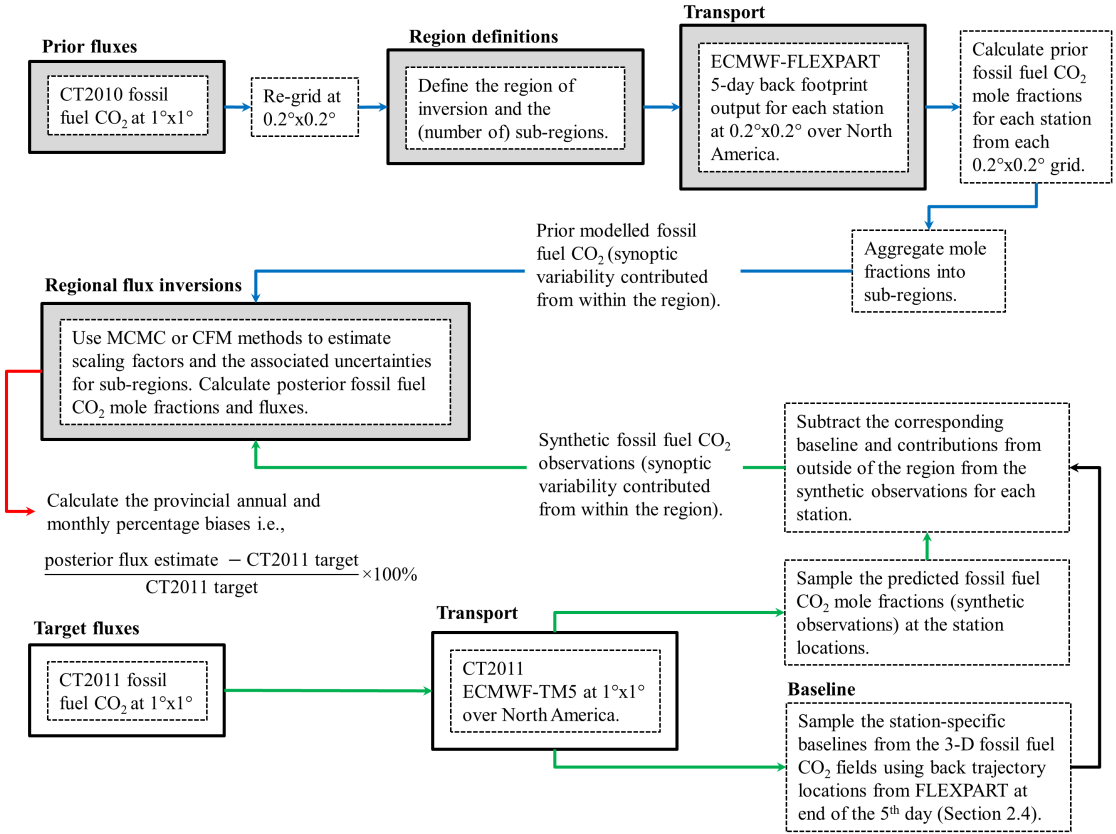

Figure 1. Schematic of the inversion experiments that have prior flux and transport errors.

ACPD
15, 22715–22779, 2015

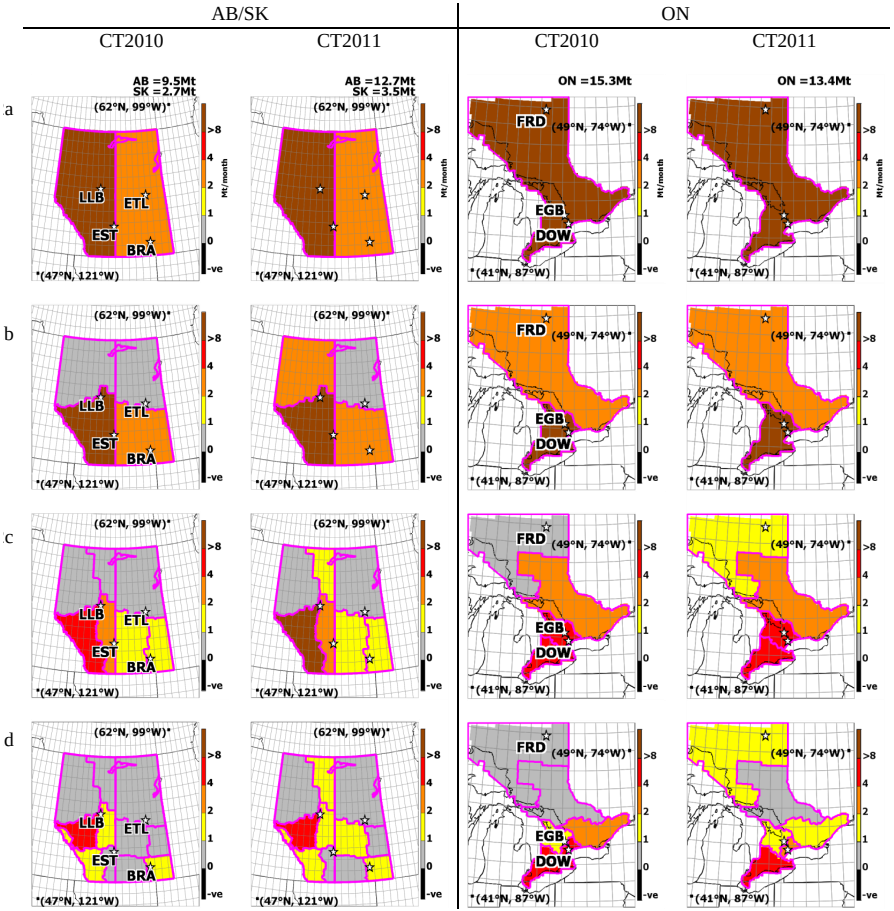

Figure 2.

ACPD
15, 22715–22779, 2015

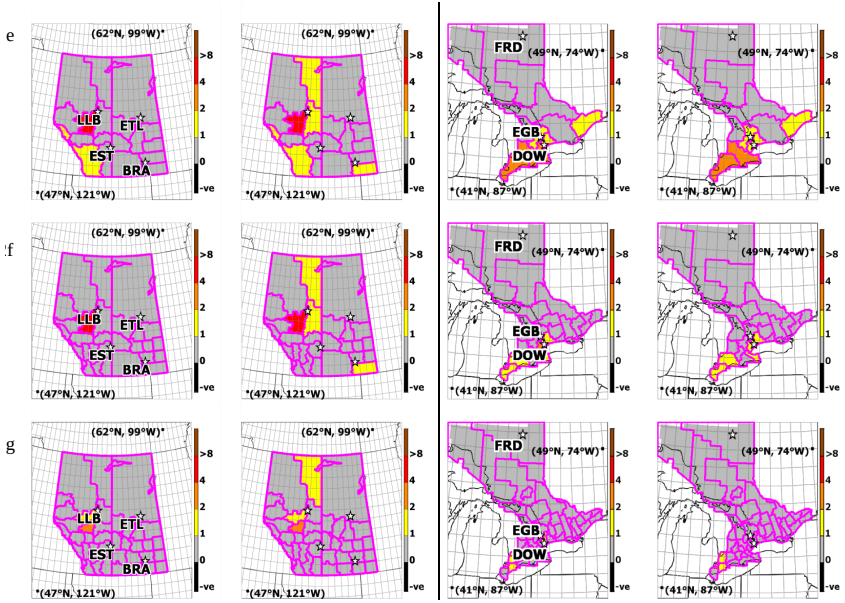

Figure 2. (a) The spatial definitions for inversion using 2 sub-regions on the left panel for Alberta/Saskatchewan (AB/SK) and 1 sub-region on the right panel for ON provinces. **(b)** 4 and 2 sub-regions for AB/SK, ON provinces respectively. **(c)** 7 and 4 sub-regions for AB/SK, ON provinces respectively. **(d)** 11 and 6 sub-regions for AB/SK, ON provinces respectively.**(e)** 19 and 12 sub-regions for AB/SK, ON provinces respectively. **(f)** 27 and 24 sub-regions for AB/SK, ON provinces respectively. **(g)** 37 and 49 sub-regions (census divisions) for AB/SK and ON provinces respectively. Sub-regional totals are color coded in Mt/month. Four stations were used in inversion experiments for AB/SK and three stations for ON shown as star symbols. Note that the northern part of the map for ON province is clipped. Examples of the fossil fuel spatial distributions of CO_2 fluxes are shown for January 2009 for AB/SK and ON obtained from the releases of CT2010 and CT2011. The January monthly provincial totals in mega-tonnes (Mt) are shown in the top right corners.

ACPD
15, 22715–22779, 2015

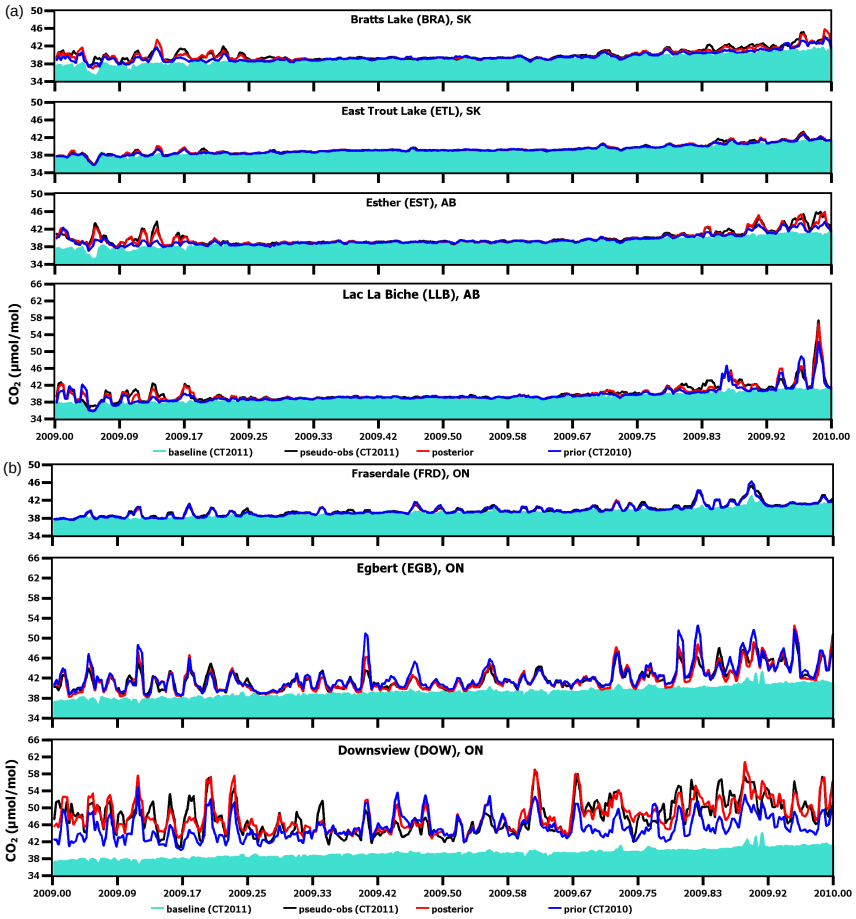

Figure 3. (a) and **(b)** model results of experiment E31 using the MCMC method for stations in AB/SK (37 sub-regions) and ON (49 sub-regions) respectively.

ACPD
15, 22715–22779, 2015

Error sources in regional inverse estimates of greenhouse gas emissions

E. Chan et al.

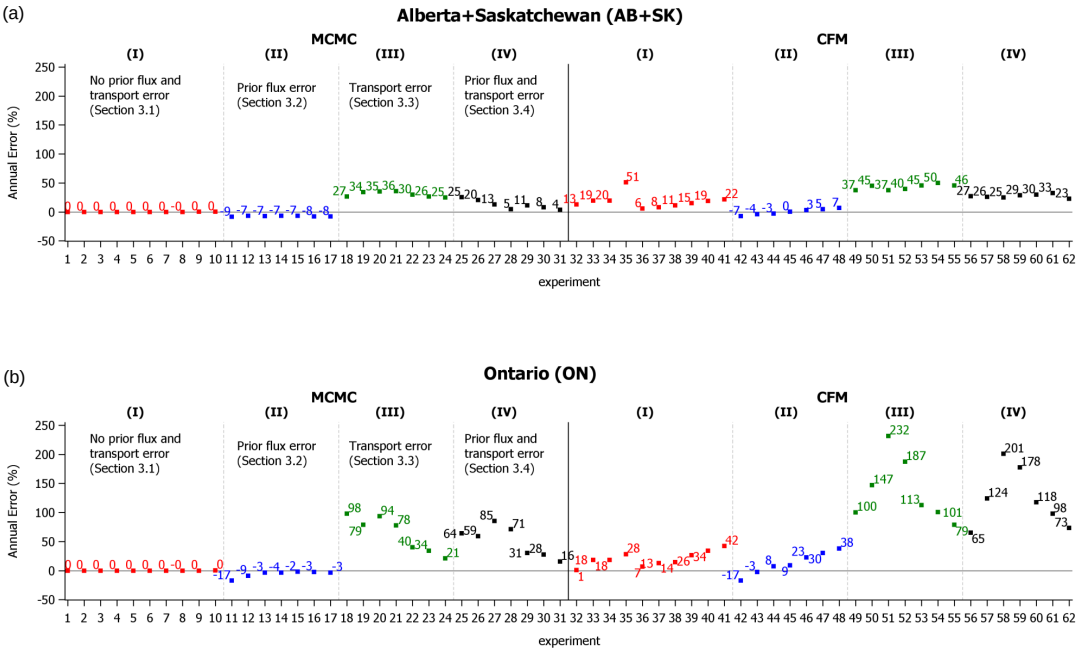

Figure 4. Annual estimation biases (relative percentage difference of the posterior estimates from the target flux) for set (I): no prior flux and transport error, set (II): flux error, set (III): transport error, and set (IV): flux and transport error cases for **(a)** provinces of AB and SK combined and **(b)** province of ON. Experiments E1–E31 and E32–E62 correspond to the results obtained from the MCMC and CFM methods respectively. See Sect. 3 for explanations of the results.

ACPD
15, 22715–22779, 2015

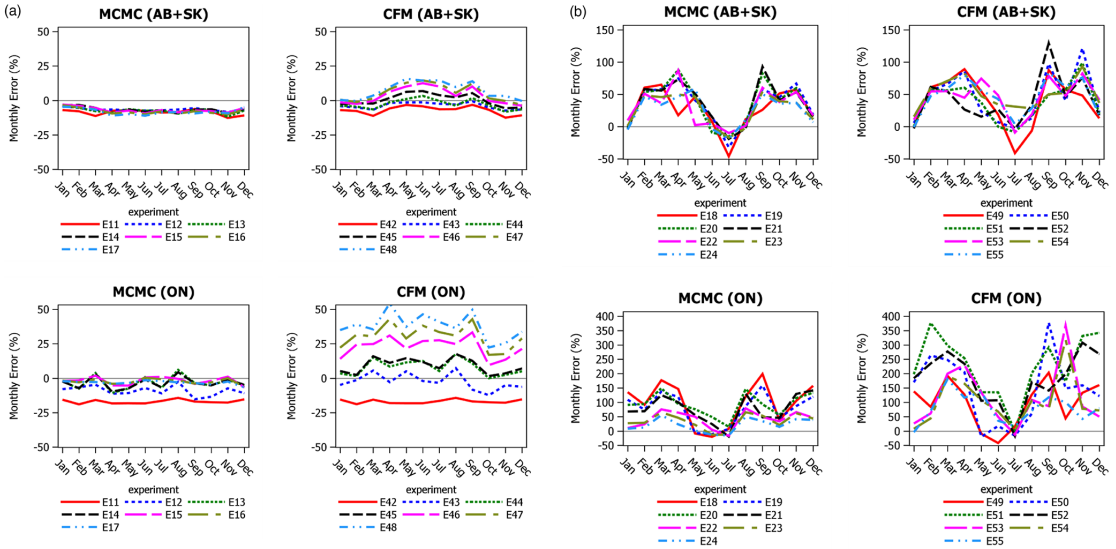

Figure 5. Monthly estimation biases (relative percentage difference of the posterior estimates from the target flux) for **(a)** flux error case and **(b)** transport error case for the provinces of AB and SK combined and province of ON. Experiments E11–E24 and E42–E55 correspond to the results obtained from the MCMC and CFM methods respectively.

ACPD
15, 22715–22779, 2015

Error sources in regional inverse estimates of greenhouse gas emissions

E. Chan et al.

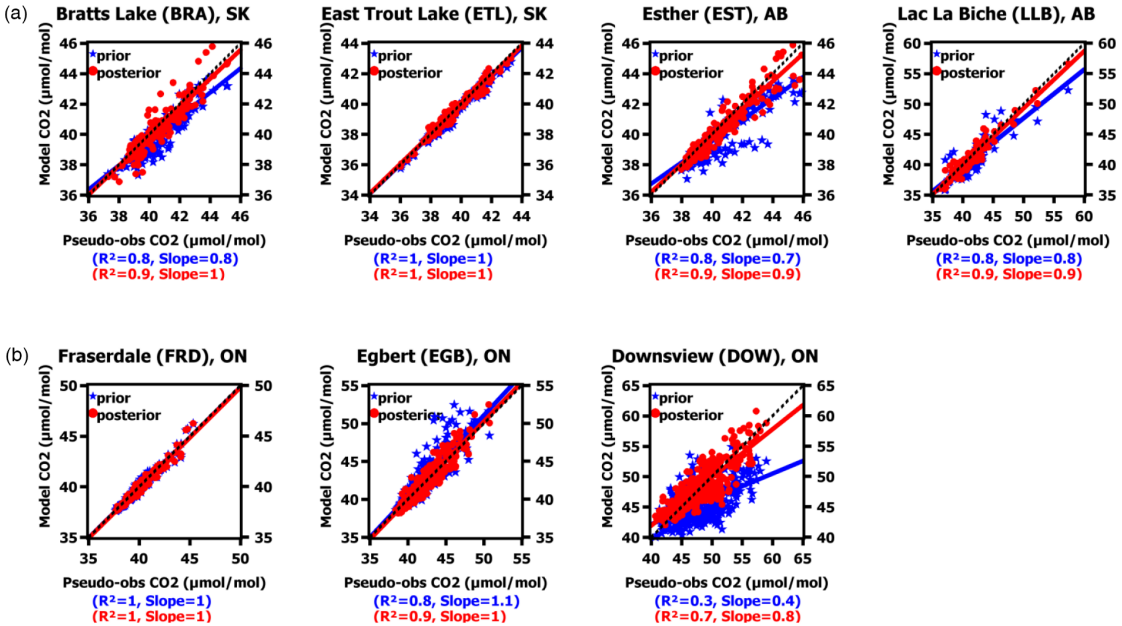

Figure 6. (a) and **(b)** linear regression analyses of experiment E31 using the MCMC method for stations in AB/SK (37 sub-regions) and ON (49 sub-regions) respectively, using January to December 2009 posterior (red) and prior (blue) results.

ACPD
15, 22715–22779, 2015

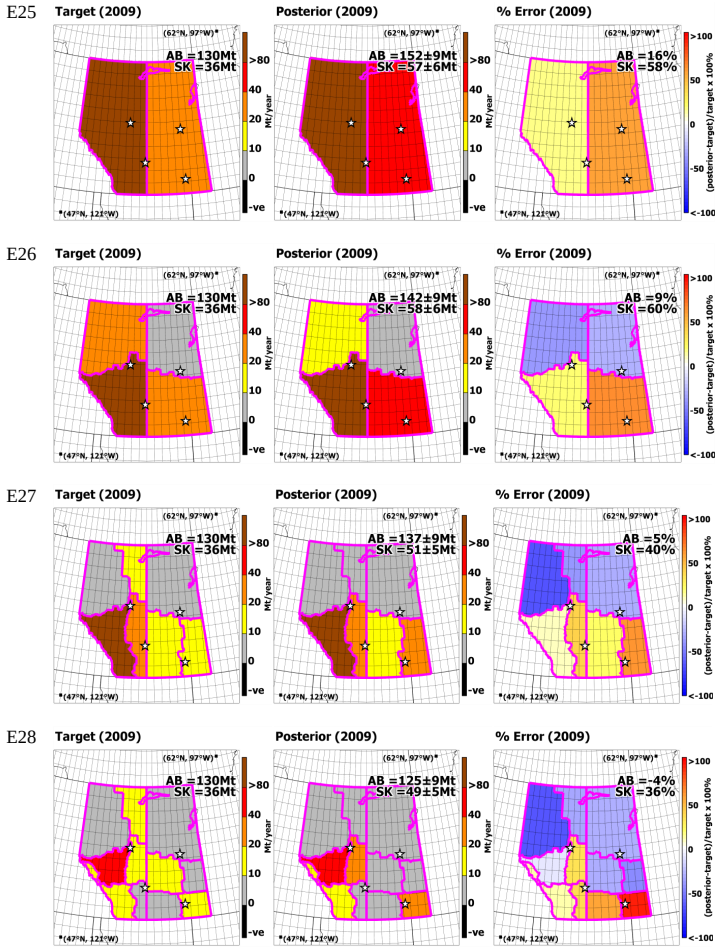

Figure 7.

ACPD
15, 22715–22779, 2015

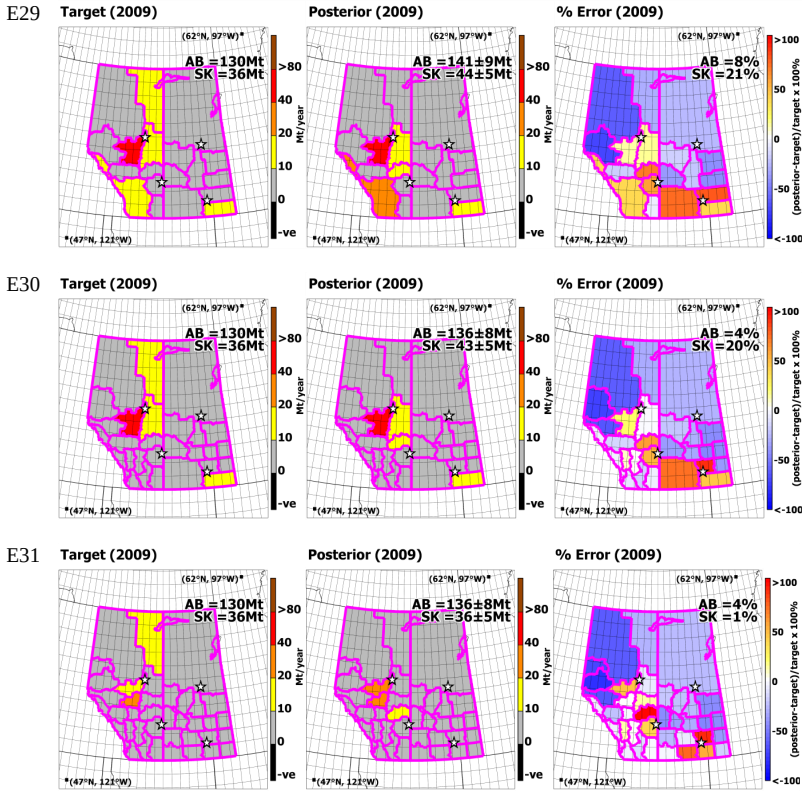

Figure 7. Annual estimation biases (relative percentage difference of the posterior estimates from the target flux) using the MCMC simulation method for the 7 spatial definitions under the conditions in which flux and transport model errors exist for the provinces of AB/SK for the year 2009. The annual provincial posterior estimates ($\pm 2\sigma$) are shown in the top right corner. Negative fluxes are shown in black.

ACPD
15, 22715–22779, 2015

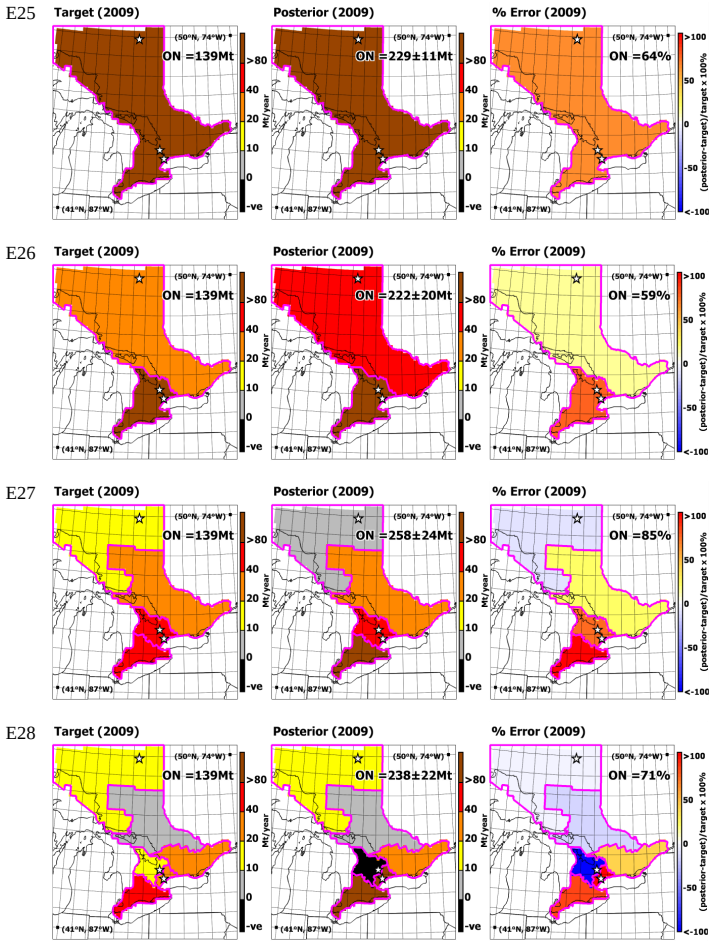

Figure 8.

ACPD
15, 22715–22779, 2015

Error sources in regional inverse estimates of greenhouse gas emissions

E. Chan et al.

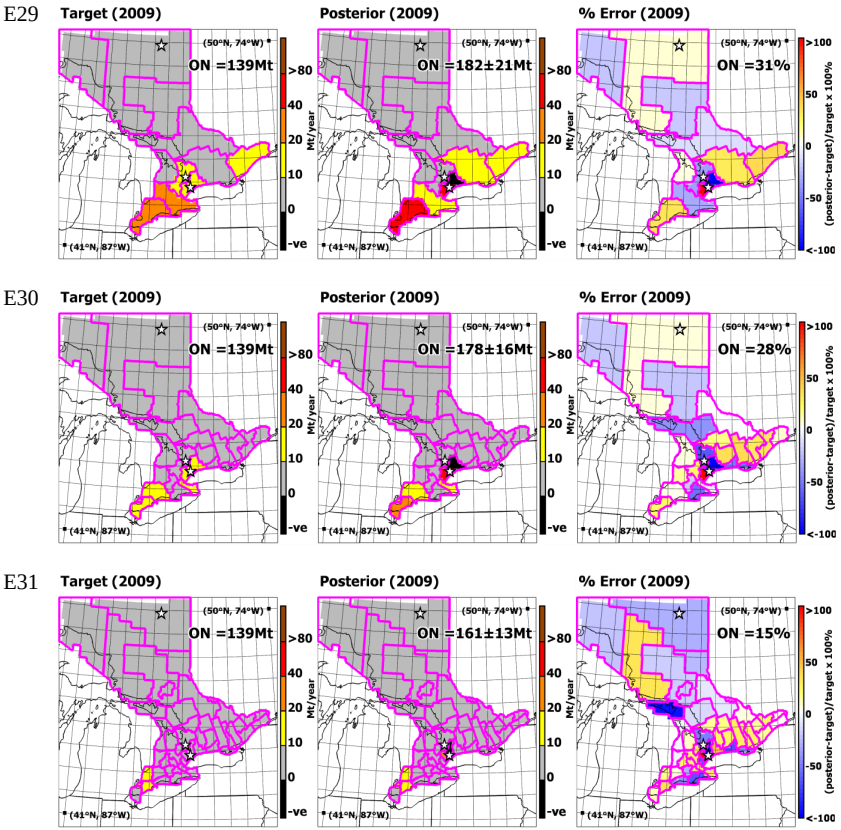

Figure 8. Same as Fig. 7 but for the province of ON.

ACPD
15, 22715–22779, 2015

Error sources in regional inverse estimates of greenhouse gas emissions

E. Chan et al.

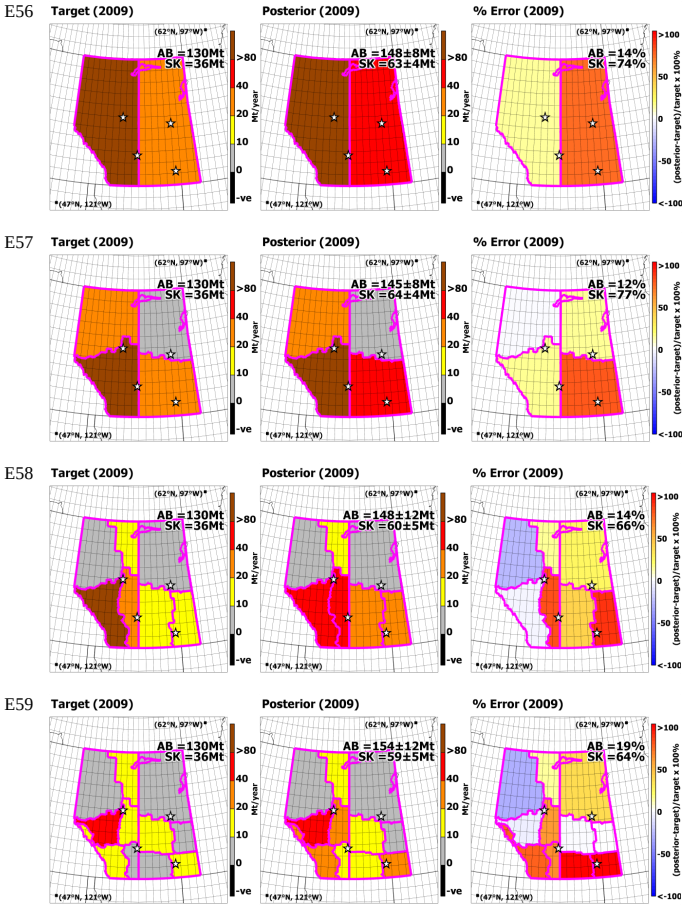

Figure 9.

ACPD
15, 22715–22779, 2015

Error sources in regional inverse estimates of greenhouse gas emissions

E. Chan et al.

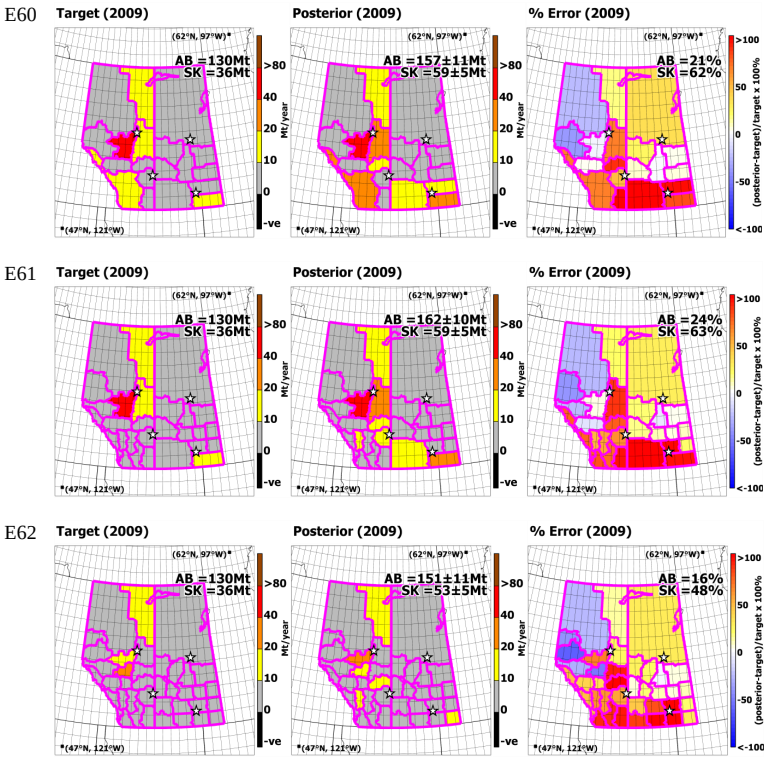

Figure 9. Annual estimation biases (relative percentage difference of the posterior estimates from the target flux) using the CFM simulation method for the 7 spatial definitions under the conditions in which flux and transport model errors exist for the provinces of AB/SK for the year 2009. The annual provincial posterior estimates ($\pm 2\sigma$) are shown in the top right corner. Negative fluxes are shown in black.

ACPD
15, 22715–22779, 2015

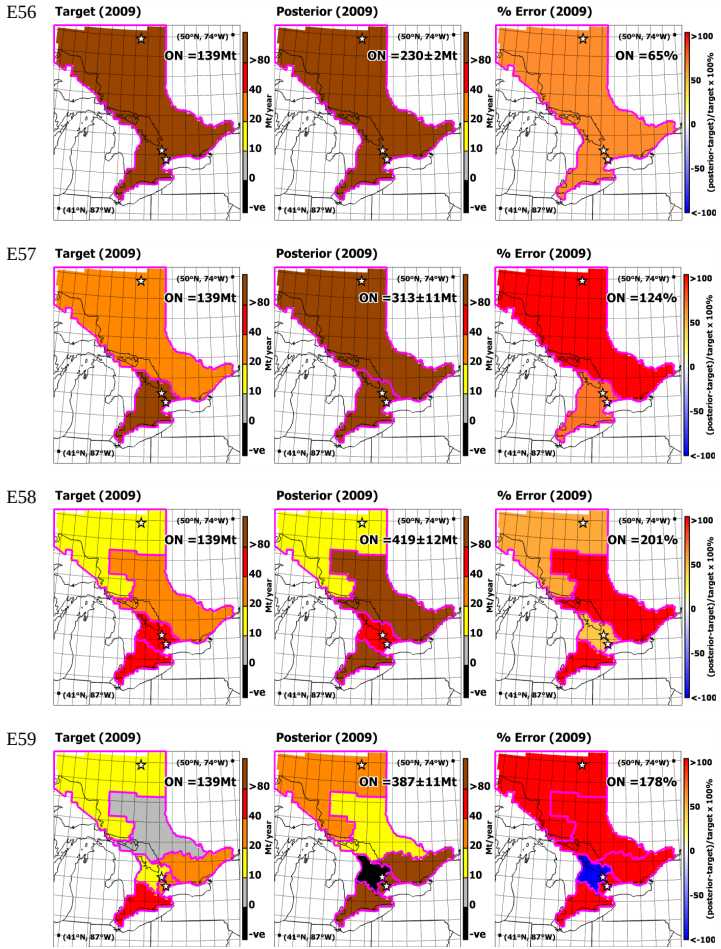

Figure 10.

ACPD
15, 22715–22779, 2015

Error sources in regional inverse estimates of greenhouse gas emissions

E. Chan et al.

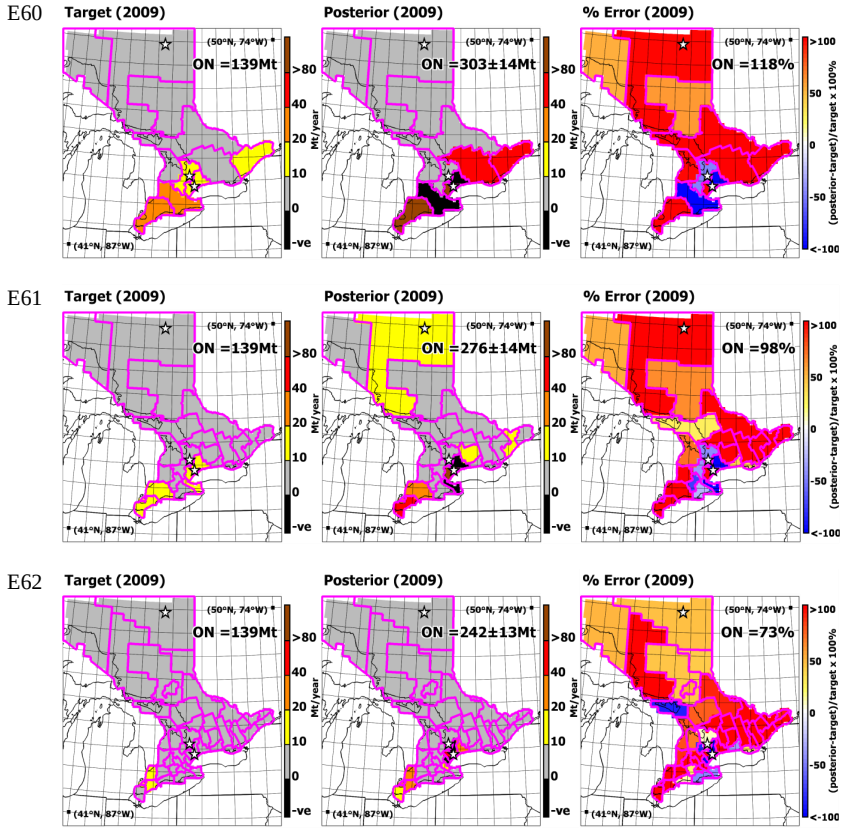

Figure 10. Same as Fig. 9 but for the province of ON.

ACPD
15, 22715–22779, 2015

Error sources in regional inverse estimates of greenhouse gas emissions

E. Chan et al.

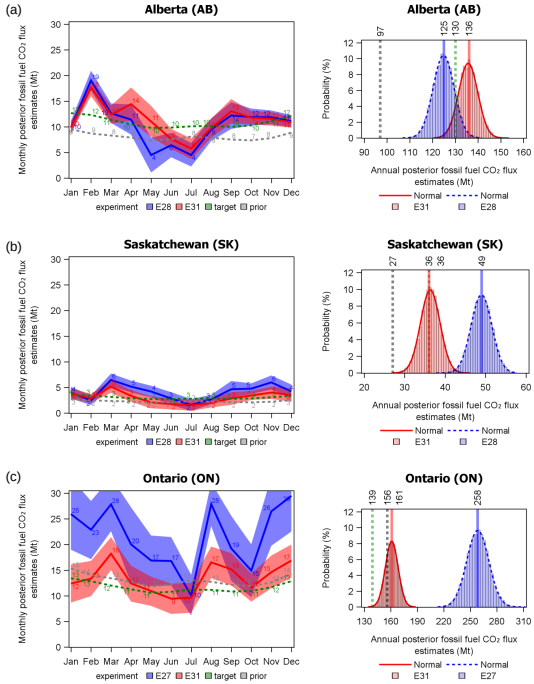

Figure 11. Monthly (left) and annual (right) fossil fuel CO_2 posterior flux estimates (in Mt) for experiments E28 (blue) and E31 (red) in comparison with the monthly prior (gray) and target (green) fluxes for the provinces of AB, SK and ON using MCMC. The monthly mean posterior estimates are shown as connecting lines. The colored bands associated with the respective experiments show the 5th and 95th percentiles of the monthly flux estimates calculated from the 10 000 MCMC simulated scaling factors for the individual months. Top right column shows the probability distributions of the annual posterior flux estimates for experiments E28 (blue) and E31 (red). The numerical values of the prior flux, annual target flux, posterior estimates of E28 and E31 are shown as vertical bars. The top **(a)**, middle **(b)** and bottom **(c)** panels show the results for the provinces of AB, SK and ON respectively.

ACPD
15, 22715–22779, 2015